A Retinal Biophysical Biomarker for Amyotrophic Lateral Sclerosis (ALS)

By

Maryam Amin Mohammed Amin

B.Sc., Ryerson University, 2016

A thesis presented to Ryerson University

in partial fulfillment of the requirements for the
degree of Master of Science

in the program of Biomedical Physics

Toronto, Ontario, Canada, 2018

Author's declaration

I hereby declare that I am the sole author of this thesis. This is a true copy of the thesis, including any required final revisions, as accepted by my examiners.

I authorize Ryerson University to lend this thesis to other institutions or individuals for the purpose of scholarly research.

I further authorize Ryerson University to reproduce this thesis by photocopying or by other means, in total or in part, at the request of other institutions or individuals for the purpose of scholarly research.

I understand that my thesis may be made electronically available to the public.

Maryam Mahdi Amin Mohammed Amin

Abstract

A Retinal Biophysical Biomarker for Amyotrophic Lateral Sclerosis (ALS)

Maryam Amin Mohammed Amin

Master of Science, Biomedical Physics
Ryerson University, 2018

Amyotrophic lateral sclerosis (ALS) is an incurable motor neuron disease with no current valid diagnostic imaging biomarkers. The retina is an extension of the central nervous system and axonal transport defects have been documented in various neurodegenerative diseases. This study reports evidence of axonal pathology in the retina of ALS patients using an interdisciplinary approach that includes the neuropathological study of retinal sections in ALS patients expanded to the optical characteristics of the whole retina preparations using eye imaging technology. The histopathological examination of retina sections revealed round profiles in the retinal nerve fibre layer in 10 out 10 ALS patients and in 4 out of 10 age-matched control patients. All 10 ALS patients showed increased phosphorylated neurofilament immunoreactivity in the retinal nerve fibre layer compared to all 10 control patients. Retinal imaging of whole globes and retina flat-mounts by blue reflectance retinal funduscopy and optical coherence tomography revealed hyper-reflective profiles in the retinal nerve fibre layer. For the first time, approximately 1μm retinal ganglion cells axons were visualized in immunofluorescence stained retina flat-mounts using near-infrared retina fundus imaging and Image Mapping Spectrometer. These findings suggest axonal pathology in retinal ganglion cells and its potential use as a novel non-invasive ocular imaging biomarker for ALS.

Acknowledgments

This project would not have been possible without the support and encouragement of multiple people. My deepest gratitude is to my thesis co-supervisor, Dr. Yeni Yucel for his unwavering support, guidance, and insight throughout this research project. I have been amazingly fortunate to have a supervisor who gave me the freedom to explore on my own and at the same time the guidance to recover when my steps faltered.

My sincere thanks go to Dr. Neeru Gupta for her guidance and support throughout the past years to make the study a well-done achievement and I am gratefully indebted for her very valuable comments on this thesis.

I further extend my personal gratitude to my co-supervisor, Dr. Carl Kumaradas as well as the members of my committee Dr. James Grafe and Dr. Yuan Xu for generously offering their time, support, guidance, and goodwill throughout the preparation and review of this document.

The members of Dr.Yucel's Lab are recognized for their help and support throughout the year and for creating an enjoyable working environment. I would like to highlight Eileen Girard for preparing the histological sections for my project. Thanks must go to Xun Zhou for always being an invaluable resource in the lab and for his time and advice. His expertise has undoubtedly helped in the completion of this thesis.

I would also like to express my appreciation to Kieran Sharma, an amazing undergraduate student who worked very diligently on the histopathological component of this study during two consecutive summers.

I would like to give special thanks to Megan Yuen, my wonderful mentee, for offering assistance on this project.

I also thank Luz A. Paczka-Giorgi for her amazing drawings for figures 1,3, and 4 of this report.

My thanks and appreciations also go to Dr.Lorne Zinman and his team from the Department of Medicine, Sunnybrook Health Sciences Center for providing post-mortem human specimens of patients with ALS.

I would also like to thank Dr. Tomasz Tkaczyk and his team at Rice University for the custom-design of the Image Mapping Spectroscopy (IMS) camera for our lab and for their support and guidance throughout this project.

I am thankful to Michael Lapinski for his expert help with IMS.

I also thank Dr. Caterina Di Ciano-Oliveira, a Biomedical Specialist at Li Ka Shing Knowledge Institute, for her technical help and support with imaging and image processing.

Very special thanks to the Henry Farrugia Research Fund for the enduring legacy of their gifts to support this project.

In addition, I would like to thank all of the faculty members in the Department of Physics that I had the privilege of interacting with during my study at Ryerson University. I truly believe that choosing Ryerson was one of the best decisions that I have ever made.

Lastly but most importantly, I would like to acknowledge my parents and siblings. I am forever in debt with their constant support, never-ending love and belief in me. I would be nowhere close to typing these words if it wasn't for their sacrifices which granted me the opportunity to pursue my interests in life. This thesis is dedicated to them.

Table of contents

List of symbols and abbreviations

+25D = +25 diopter
+90D = +90 diopter
ALS = Amyotrophic lateral sclerosis
ALSFRS-R = Amyotrophic lateral sclerosis functional rating scale-revised
AMD = Age-related macular degeneration
AOSLO = Adaptive optics scanning laser ophthalmoscopy
ART = Automatic Real Time
BAF = Blue autofluorescence
BR = Blue reflectance
CAP-Gly = Cytoskeleton-associated protein, glycine-rich
CCD = Charge coupled device
CNS = Central nervous system
cSLO = Confocal scanning laser ophthalmoscopy
c9orf72 = chromosome 9 open reading frame 72
DAPI = 4',6'-diamino-2-phenylindole
DTI = Diffusion tensor imaging
EMG = Electromyography
FA = Fundus angiography
FAF = Fundus autofluorescence
GCL = Ganglion cell layer
H&E = Hematoxylin and eosin
HRA = Heidelberg Retina Angiography
ICGA = Indocyanine green autofluorescence
ILM = Inner limiting membrane
INL = Inner nuclear layer
IPL = Inner plexiform layer
IMS = Image mapping spectrometer
IOP = Intraocular pressure
IR = Infrared reflectance
IRAF = Infrared Autofluorescence
LC = Lamina cribrosa
MColour = Multicolour Reflectance
MRI = Magnetic Resonance Imaging
NDD = Neurodegenerative diseases
NF = Neurofilament
NF-H = Neurofilament heavy chain
NF-L = Neurofilament light chain
NF-M = Neurofilament medium chain
NIRF = Near-infrared fluorescence
NIRFOI = Near-infrared fluorescence ocular imaging
OCT = Optical coherence tomography
ONH = Optic nerve head
ONL = Outer nuclear layer
OPL = Outer plexiform layer

PAS = Periodic acid-Schiff
P-NF = Phosphorylated neurofilament
PNS = Peripheral nervous system
PBS = Phosphate buffer saline
PET = Positron emission tomography
PRL = Photoreceptor layer
ROI = Region of Interest
RNFL = Retinal nerve fiber layer
RPE = Retinal pigment epithelium
RT = Room temperature
SD-OCT = Spectral-domain optical coherence tomography
SMI31 = Mouse anti- phosphorylated neurofilament H antibody
SOD1 = Superoxide dismutase 1
TD-OCT = Time-domain optical coherence tomography
TDP-43 = TAR DNA-binding protein 43
y/o = years old
μ_a = Absorption coefficient
μ_s = Scattering coefficient

List of tables

List of figures

1. INTRODUCTION

1.1. Nervous system

The nervous system is composed of two parts, the central nervous system (CNS) and the peripheral nervous system (PNS). The CNS consists of the brain and the spinal cord and PNS consists of sensory and motor neurons that connect the CNS to peripheral tissues such as skin and muscle. The retina [2] and the optic nerve [3] are integral parts of the CNS. Neurons are the basic cellular unit of the nervous system. A neuron is composed of the cell body, dendrites, which are cell processes that receive the neural signal from other neurons, and the axon, a process that conveys the information to target neurons. The function of the axon is the transmission of the neural signal across its length from the cell body to the target neuron. Interneurons have short axons confined to an anatomical structure, while projection neurons have long axons that convey the signal to target neurons in a distant anatomical structure [2, 4]. Sensory neurons and motor neuron are two functional major types of neurons. Sensory neurons or afferent neurons bring information from sensory receptors to the CNS structures for further processing. Motor neurons or efferent neurons convey the neural signal from CNS to effectors such as muscle fibers.

1.1.1. Axons and axonal transport

Axons are cellular processes originating from the cell body and extending to the axon terminal that terminates on target neurons or effector structures such as skeletal muscle fibers. In the CNS, the electrical signal travels along the axons that are insulated by the myelin sheath that is synthesized by oligodendrocytes. Myelination provides stability for

rapid signal propagation [5]. The combined signal effects from dendrites are summed and travel through the hillock where action potentials are generated. The action potential is conveyed along the axon to the axon terminal. This process relies heavily on the polar characteristic of axons since the potential is driven forward when there is a steep voltage gradient between the current position of the action potential and the region ahead. Since the flow of charged ions is restricted to the nodes of Ranvier when the myelin sheath is absent, there is a lower energy input needed for the generation and maintenance of the voltage gradient [6]. Once the signal reaches the axon terminals, the neurochemical transmitter is released or other ways of synaptic activation will be triggered at the post-synaptic receptors of the target neurons.

All axons contain structural molecules which form a scaffold. The neurofilaments are intermediate filaments of the neurons and maintain the structure of the neurons. Several groups have shown that disruption of neurofilaments can induce their accumulation in the neurons (Figure 1), and this can damage the motor neurons to produce symptoms bearing many similarities to ALS [7-9]. Tubulins are the building blocks of microtubules, another component of the axon's scaffold. Researchers have found several mutations in proteins associated with microtubules that produce motor neuron diseases [10, 11].

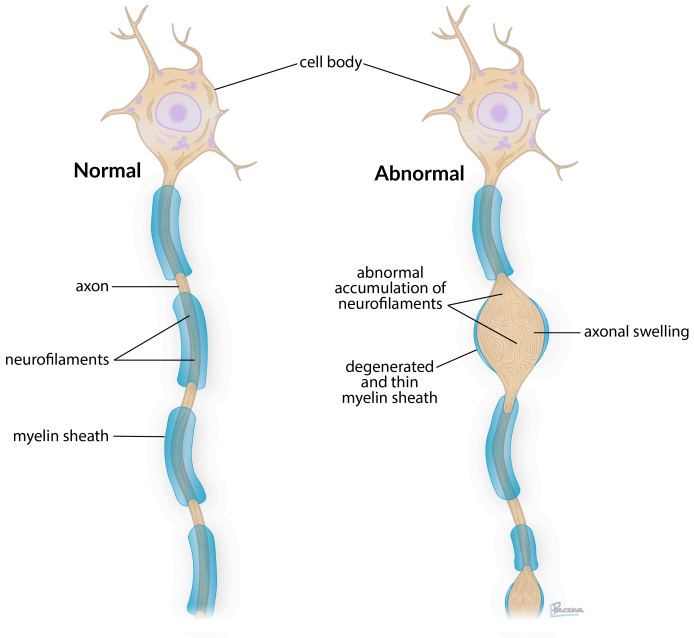

Figure 1. Normal vs. abnormal axon

Abnormal neuron is showing swollen segments of the axon and abnormal accumulation of neurofilaments.

Axonal transport has a critical role in the maintenance and homeostasis of healthy neurons. Without which, neurons with long axon will not be able to get the necessary nutrients at their terminals and repair damages in a timely manner. Cytoskeletal motor proteins like kinesins and dyneins are responsible for the movement of cargos in the two types of axonal transport, namely the anterograde transport and the retrograde transport [12]. The anterograde transport refers to the movement of materials from the cell body to the terminals. The cargos in this plus-end-directed movement usually consist of newly synthesized organelles, proteins, and synaptic components. On the other hand, the retrograde transport refers to the movement of materials in the opposite direction. The cargos in this minus-end-directed movement typically consist of damaged organelles to be degraded and recycled. Kinesins and dyneins work with other molecules to form

protein complexes to mediate the movement of cargos (Figure 2) [13]. For example, dynactin binds to dynein directly to form a dynein-dynactin complex which has several subunits. $p150^{Glued}$ is the subunit responsible for microtubule-binding. A cytoskeleton-associated protein, glycine-rich (CAP-Gly) motif can be found within this subunit that contributes to the microtubule-anchoring activity. By phosphorylation and protein-binding at CAP-Gly, the dynein-dynactin complex may be more or less likely to bind to the microtubules [14]. Axonal transport is closely regulated. Defects in any proteins or filaments that play a role in axonal transport can lead to inefficient homeostasis that is necessary for healthy neurons to function and abnormal accumulation of proteins and organelles. In general, protein aggregation, glutamate excitotoxicity, oxidative stress, and mitochondrial dysfunction are several mechanisms proposed to underline the motor neuron degeneration [15, 16].

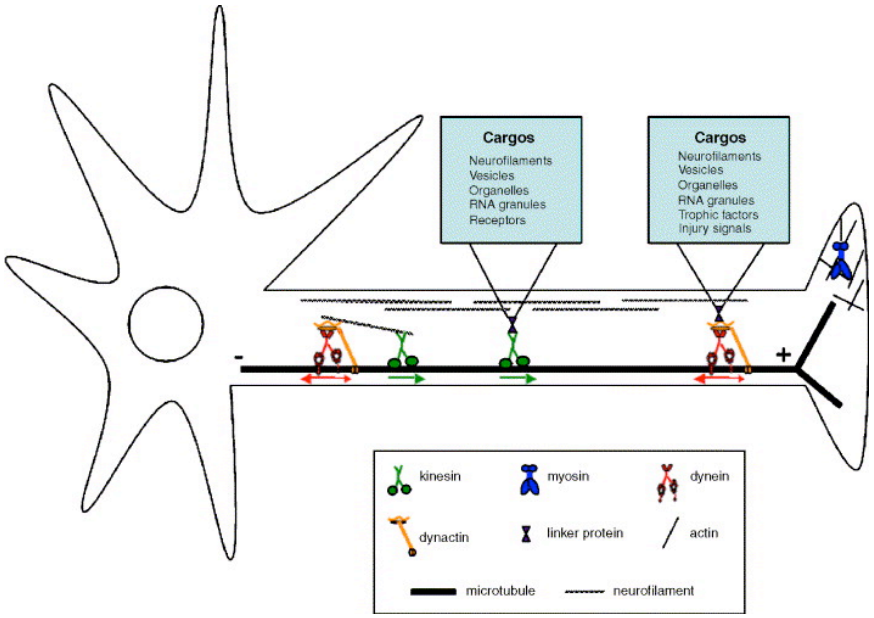

Figure 2. Axonal transport in neuron

Cytoskeleton motor proteins such as kinesin and dynein are responsible for movement of cargos such as proteins and organelles along the axons. Kinesin is responsible for anterograde (green arrows) while dynein is responsible for retrograde transport in (red arrows) [1]

1.1.2. Axonal transport defect in neurodegenerative diseases

Axonal transport defects had been documented in numerous neurodegenerative diseases (NDD) [17-19]. Several lines of evidence suggest that the axonal transport defects results in NDD or are the consequences of these diseases [20, 21]. To find out whether axonal transport disruption alone can lead to motor neuron degeneration, LaMonte and his team engineered a transgenic mouse that over-expresses dynamitin, making the dynactin defective and decreasing rate of retrograde axonal transport. Compared to wild-type mice, these transgenic mice had significantly weaker muscle strength, lower stamina and greater loss of motor neurons. Neurofilament accumulation was also observed in the peripheral nerves of these transgenic mice. As the transgene was introduced postnatally in this study, the loss of neurons was interpreted as due to the inhibited transport of the mature axons rather than a developmental anomaly.[16]

In another study by Stokin and his team, axonal blockages and swellings were observed in the early stages of the disease in a transgenic Alzheimer's disease (AD) mouse model. Axonal pathology in this model was observed before any amyloid deposition, a pathological hallmark of AD. Based on this finding, the authors suggested that an axonal injury which would lead to defective axonal transport has a causal role in the pathogenesis of AD. [17]

Glaucoma is a neurodegenerative optic neuropathy disease that is often associated with elevated intraocular pressure (IOP) [22]. In glaucoma rat model with moderate IOP elevation that was used to explore the role of axonal injury in the retinal ganglion cells [22], axonal damage at the optic nerve head and disrupted anterograde fast axonal transport were observed. However, the chronology of nerve damage and axonal transport

defects was not addressed in this study. With insufficient evidence fully supporting either side of the argument, it is still unclear whether axonal transport defect is the cause or the consequence of neurodegeneration. Nevertheless, axonal transport is an integral component of the pathological processes implicated in neurodegenerative diseases.

1.1.3. Neurofilament transport

The neuronal cytoskeleton is made up of various components, one of which being intermediate filaments. Together with other filaments and tubules, they provide neurons with the necessary structural support for conduction of electric signal [23]. Neurofilament (NF) is a type of intermediate filament that is highly abundant in the axonal processes and critical for maintaining axonal diameter and caliber [8]. The three neurofilament subunits NF-L (light chain), NF-M (medium chain), NF-H (heavy chain) assemble together to form a functional NF molecule. Phosphorylation and dephosphorylation of NF govern various aspects of axonal transport. For example, phosphorylation at the amino-terminal heads of the NF-M and NF-H subunits will bring the NF to a stationary phase and form a lattice structure with their phosphorylated sidearm [24]. Approximately 90% of all NF is at the stationary phase to provide the axonal volume and diameter for healthy neurons. The overall rate of axonal transport may fluctuate depending on the degree of phosphorylation as well as interactions between the stationary and moving NF. [7]. In addition, the movement of individual neurofilament molecules can be divided into slow or fast axonal transport. Intermittent pauses were observed for slow neurofilament transport, without which the overall rate of movement will be the same for both [25, 26].

During these pauses, neurofilaments are phosphorylated and affinity to motor proteins decreases, immobilizing these molecules. Axonal transport of neurofilament may be resumed following dephosphorylation of the subunits.

1.2. Retina, an extension to the central nervous system

During embryonic development, the retina and optic nerve extend from the diencephalon thus, the retina has been considered an extension of the central nervous system (CNS) [27-31]. The unmyelinated axons in the retinal ganglion cell layer converge toward the optic disc and form the optic nerve at the back of the eye. The retinal ganglion cell axons that become myelinated at the optic nerve conveys the visual information from the eye to the relay visual stations in the brain. Several studies investigated the correlation between neurodegeneration in the CNS and thinning of the retina [32, 33]. Because of the availability of non-invasive imaging through the eye, the retina is considered as a window to study neurodegenerative diseases affecting the brain [27].

1.2.1. Retina anatomy and function

The retina is a multi-layered neural tissue that lines the inner surface of the eye. The layers are responsible for different functions. Photo-transduction, initiated by light, is carried out by rod and cone photoreceptors located in the photoreceptor layer. Visual signals are further passed along to bipolar cells in the inner nuclear layer. Eventually, they reach the retinal ganglion cells and their axons located in the retinal nerve fibre layer [34]. Retinal thickness varies across the whole surface, from 400μm around the optic

nerve head and to 140μm at the ora serrata, in the peripheral retina. The macula that is largely responsible for visual acuity, has a thickness of 350μm at the periphery and 140μm at the foveola [34]. The decrease in retinal nerve fibre layer thickness is usually associated with normal aging or ocular diseases like glaucoma [35, 36].

1.2.2. Retina pathology

Due to the complexity and multilayered characteristic of the retinal tissue, different pathological processes are involved in retinal diseases. Some of the most relevant pathological hallmarks include retinal ganglion cell degeneration in glaucoma, loss of photoreceptors and choroidal neovascularization in age-related macular degeneration (AMD) and pathology of blood vessels in diabetic retinopathy [37, 38].

1.3. Neurodegenerative diseases

Neurodegenerative disease is a group of heterogeneous disorders and affects the CNS. It causes progressive nervous system dysfunction and it is characterized by loss of neurons. It is associated with atrophy of the affected nervous structures. The prevalence of neurodegenerative disorders is increasing, partly due to aging, and to the lack of effective treatments [39]. Alzheimer's disease, Parkinson's disease, Huntington's diseases, and ALS are a few examples of neurodegenerative diseases. In this study, we focused on ALS disease and the axonal pathology and optical characteristics in the retina of ALS patients.

1.3.1. Amyotrophic lateral sclerosis (ALS)

ALS is an incurable neurodegenerative disease, commonly characterized by a gradual degeneration of upper and lower motor neurons. Symptoms include muscle atrophy and weakness as well as difficulty in speaking, swallowing, and breathing. ALS results in death within 2-5 years after clinical onset due to respiratory failure from weakness of diaphragm muscle [40-44]. Phenotypically, ALS is mainly classified as limb-onset and bulbar-onset. In about 70% of the cases, symptoms begin in the arms or legs, referred to upper limb- and lower limb- onset, respectively. About 25% of the cases are bulbar-onset, in which symptoms appear as difficulty speaking and swallowing. Bulbar-onset is followed by limb-onset in later stages of the disease. The remaining 5% of the cases have initial trunk or respiratory involvement [45]. ALS level of disability and status is measured by series of questionnaire-based scale, from zero to 4, known as ALS functional rating scale (ALSFRS). The scale measures physical function in carrying out activities of daily living such as speech, swallowing, salivation, handwriting, walking, dressing and more. Zero scale is complete disability and 4 is normal [46]. Due to the short life expectancy after onset of the symptoms, an early and precise diagnosis of this disease is crucial [40]. There have been numerous studies dedicated to finding a valid biomarker [47]. Unfortunately, due to the heterogeneous nature of this disease, neurologists still rely on clinical diagnostic criteria to differentiate ALS from ALS mimicking diseases [48].

1.3.1.1. Causes of ALS

ALS can be familial or sporadic. However, the two forms of this disease share similar phenotypical characteristics [49]. It still remains unclear whether they share the same pathogenesis. There have been multiple proposed mechanisms from previous studies [50]. Among which, mutations in the superoxide dismutase 1 (SOD1) is one of the most commonly discussed genetic causes [51-53]. Superoxide dismutase is an enzyme responsible for catalyzing the partitioning of superoxide anion radical. The misfolded mutant protein is toxic and the accumulation of which could lead to mitochondrial dysfunction and defective axonal transport, both of which are critical for the proper functioning of neurons [54]. Mutation in the C9orf72 gene is another mechanism thought to be contributing to the pathogenesis of ALS. This gene has a critical role in normal microglial function, which is implicated in neuroprotection. There has been evidence suggesting an expansion of a hexanucleotide repeat (GGGGCC) in the first intron/promoter region of the C9orf72 gene to cause both ALS and frontotemporal dementia [55]. Aside from genetic causes, the abnormal aggregation of ubiquitinated TAR DNA-binding protein (TDP-43) has been proposed to cause motor neuron degeneration [56]. It is beyond the scope of this thesis to list out all the proposed causes of ALS due to its heterogeneity. However, it is safe to say that there is a lot about the pathogenesis of this disease that is not clearly understood.

1.3.1.2. Diagnosis of ALS and imaging

Due to a lack of valid biomarkers, the diagnosis of ALS is dependent on clinical criteria to rule out the other diseases that mimic ALS. The El Escorial World Federation of Neurology designed diagnostic criteria used by clinicians worldwide [48]. Most of the time, it is applied after patients show signs of upper or lower motor neuron degeneration, a hallmark of ALS. Typically, physicians will proceed with electrophysiological examination, neuroimaging or other lab tests [48].

Electromyography (EMG) is one of the first tests to be performed. It can detect electrical activity of muscle fibers as well as speed and strength of signals, which can tell about nerve dysfunction and problems with the nerve-to-muscle signal conduction. By analyzing the results, physicians would differentiate ALS from other motor neuron diseases like motor neuropathy. MRI scans are used to image the brain and the spinal cord to rule out the presence of tumours or other abnormalities that could also lead to the muscle weakness [48]. Diffusion tensor imaging (DTI) is another neuroimaging modality used in examining neuronal injury by measuring diffusion of water molecules. DTI allows in-vivo non-invasive imaging of tissue microstructure and has shown surrogate markers of axonal damage and demyelination [57, 58]. Imaging modalities are coupled with other tests to help diagnose and understand the disease process. Laboratory tests are usually performed to look at the amount of proteins such neurofilament in the blood. [48] Again because of the heterogeneous nature of the disease, a series of clinical tests are needed to be repeated to confirm the diagnosis made by the physician. Limitations on the current diagnostic criteria as well as future directions have been addressed often in recent

research [47, 50, 59]. Due to the short life expectancy after symptom onset, it is of our greatest priorities to search for valid biomarkers for earlier and more precise diagnosis.

1.3.1.3. Treatment of ALS

Currently, there is no cure for ALS. Treatment often aims at extending the life expectancy of patients as well as improving the remaining quality of life. Riluzole, an FDA-approved drug commonly used in the therapeutic treatment of ALS [47]. It is an anti-glutamatergic drug and acts on the excitotoxicity due to excessive glutamatergic stimulation [60]. This treatment has been shown to slow down disease progression and lead to an increase of approximately 2-3 months in life expectancy [61]. Unfortunately, due to the complexity of the disease, the available treatment options are extremely limited.

1.4. Optics of the eye

The eye is a complex organ with a very unique structure, allowing it to transmit and detect the light and transform it into a visual signal. The eye is comprised of few layers and components (Figure 3) where they all work together to focus the light onto the retina and form image. When the light hits the retina, neurons in the eye are stimulated and neural signals are generated and sent to the brain. The brain further processes the visual signal and enables the vision.

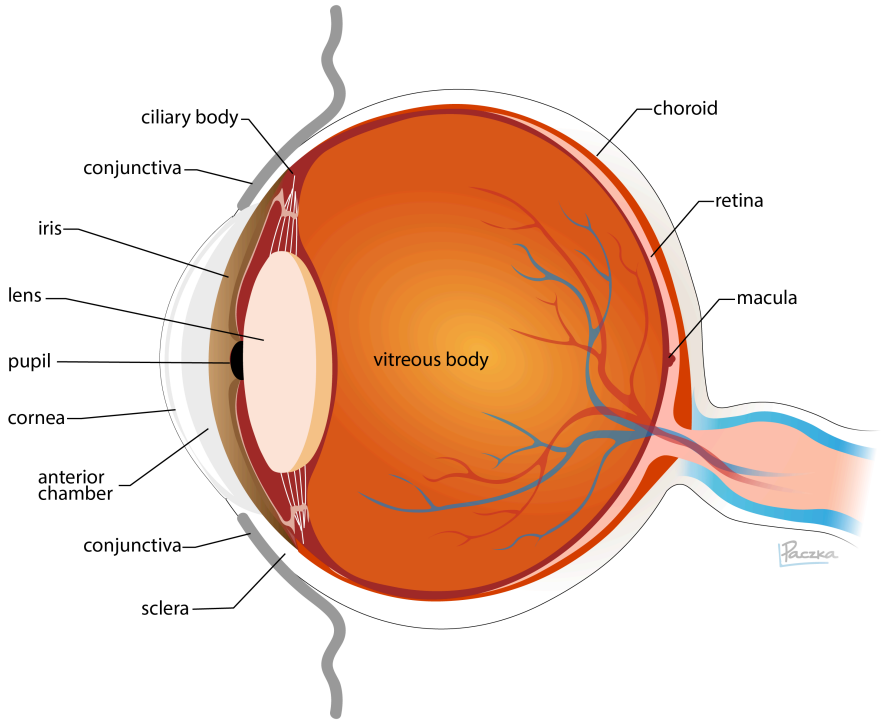

Figure 3. Human eye with various anatomical structures

The eye is made of three major layers. The outer layer includes the cornea and sclera. The middle vascularized and pigmented layer is called the uvea, and it consists of the iris, ciliary body and the choroid. The inner layer is the retina. The cornea and the lens help focus the light on the retina.

The light enters the eye through the transparent cornea, reaches the pupil. The iris controls the size of the pupil by dilation and constriction and the amount of light entering the posterior pole of the eye [62].

The power of the lens adjusts the focal point and accommodates different object distance. The lens and cornea work together to bend and focus the light on the retina at the fovea. The fovea is a temporal region of the retina that is responsible for the central vision with high visual acuity where the retina layers above the fovea are discontinued allowing the light transmission to photoreceptors. The focused light on the fovea has an energy density (J/cm^2) about 10^5 larger than the collimated light. Therefore, light delivering a radiant exposure insufficient to produce skin damage may indeed cause injury when focused on the retina. This is why the laser damage threshold for the eye is much lower than the skin and other tissue [63].

Although light is essential for vision, depending on its wavelength and the exposure duration it could cause damage to the retina. Ultraviolet, visible, and infrared light are portions of the electromagnetic spectrum, called optical radiation band, that particularly interact with the eye. Ultraviolet and infrared light are further divided based on their photon energy, tissue penetration, and bio-effects. The visible light is subdivided based on the visual function [63]. Table 1 summarizes the wavelength range in optical radiation band and its subdivisions.

Table 1. Bands of electromagnetic spectrum interacting with the eye

Optical radiation band	Optical radiation sub-bands
Ultraviolet (UV; 100-400 nm)	**UVC (100-260 nm)**
	UVB (260-315 nm)
	UVA (315-400 nm)
Visible (VIS; 400-700 nm)	**Short wavelength (blue)**
	Medium wavelength (green)
	Long wavelength (red)
Infrared (IR; 700-10,000+ nm)	**IRA (700-1400 nm)**
	IRB (1400-3000 nm)
	IRC (3000-10,000+ nm)

Different optical radiation bands with their relative propagation through the ocular tissue are shown in figure 4. The cornea, aqueous humour, lens, and the vitreous humour are transparent to visible (VIS) and IRA wavelengths. Therefore, excessive VIS and IRA may damage the retina and choroid. UVC and UVB get absorbed by nucleotides and aromatic acids and do not penetrate beyond the cornea and lens. IRB and IRC wavelengths are absorbed by water molecules and do not penetrate past the cornea. These wavelengths of light could damage the surface tissue of the eye such as the conjunctiva and the cornea [63].

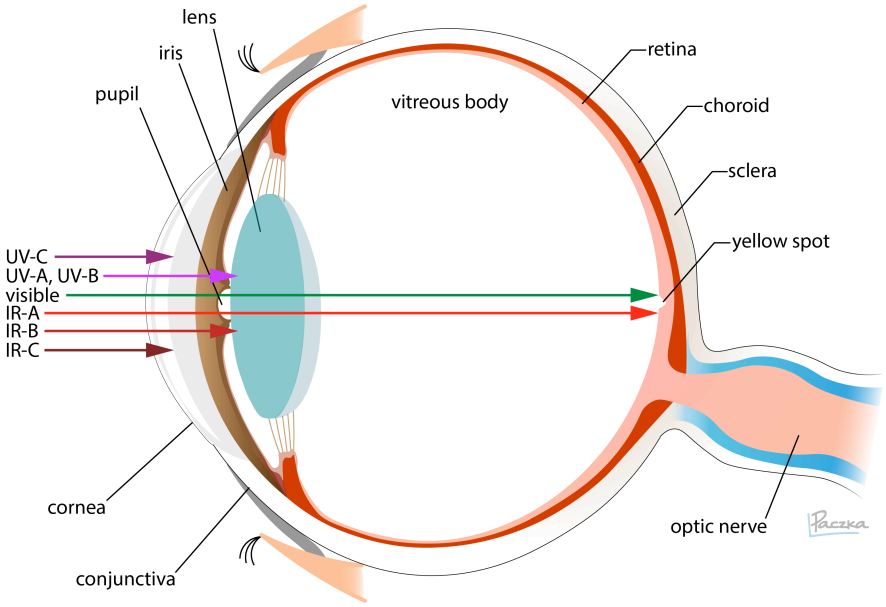

Figure 4. Propagation of various optical radiation bands through the eye.

Abbreviation: UV= Ultraviolet; IR= Infrared

The absorption and scattering properties of the tissue depend on the wavelength of the light propagating through the tissue. Knowing the absorption and scattering properties of the tissue components such as nucleic acid, proteins, lipids and endogenous pigments one can determine the tissue volume, or optical zone, affected by the light exposure. Photon absorption is proportional to the cross-sectional area of the absorbers and their density in the tissue. The larger cross-sectional area of the absorber, the more likely they will intercept a photon. Scattering happens when the photons deflect due to change in the reflective index from one medium to the other or due to interactions between the photon and particles in the medium [62].

Research has shown retina has the highest value of absorption coefficient (μ_a) and scattering coefficient (μ_s) due to the high concentration of photopigments in the rods and cons [64]. Photopigments interact with visible light to trigger the neural pathway associated with sight. They can also scatter in the infrared region [65]. These features have been used to trigger events in the retina by mapping changes in the infrared reflectance [66]. The hemoglobin present in the vasculature behind the retina does not interact strongly with infrared light, allowing the infrared reflected signal to truly present photochemical signaling in the retina [66, 67]. Compared to the lens and retina, the cornea is slightly more absorbent and less scattering occurs as wavelength reaches to infrared. The lens absorbs weakly in lower infrared regions compared to the higher region but, the scattering coefficient increase from 950-1000 nm and at the lower infrared region is constant. The retina has almost similar trends as the lens, where μ_s increase and μ_a decrease slightly towards infrared [64]. Comparing the absorption and scattering coefficients of the ocular tissue in the visible and infrared region suggest the cornea has lower μ_a and μ_s in the near-infrared compared to the visible region. Also, the lens and the retina have similar μ_a value in the near-infrared and visible range. The μ_s value in the retina is slightly lower in near-infrared compared to the visible region and in the lens is slightly higher in near-infrared than the visible region [64, 68]

1.5. Retinal imaging

As described in the previous sections, the retina is a multi-layered neural tissue lining the interior part of the eye. For image formation on the retina, the ocular structures along the optical path including the retina have to be transparent. The retina converts the incoming light into neural signals and processes and conveys them to the optic nerve and then to the central visual centers in the brain. The anatomy of the eye and the transparent structures in the optical path to the retina makes the retina, and thereby CNS tissue, to be accessible for non-invasive imaging techniques. The retina is a metabolically active tissue with a double blood supply which can be used to study blood circulation. Therefore, because of the retina's architecture, dictated by its function, a disease of the eye, as well as diseases affecting the brain and blood circulation, may be monitored in the retina using non-invasive imaging techniques. This makes retinal imaging and analysis a great candidate not only for eye diseases but also for diseases affecting the brain and blood circulation.

During the last century, retinal imaging technologies have developed rapidly and have become more commonly used in the clinical setting. Retinal specialists use fundus photography to keep track of the retinal condition of patients. Any detected abnormalities will lead to further investigation and diagnosis of diseases. It is mostly used for blinding eye diseases such as diabetic retinopathy, macular degeneration, glaucoma [69] and determining of cardiovascular risk factors such as stroke, hypertension or myocardial infarct [69-71]. Optical Coherence Tomography (OCT) and fluorescein angiography are other retinal imaging techniques used in the diagnosis and management of patients with inflammatory retinal diseases, macular degeneration and diabetic retinopathy [69].

1.5.1. Confocal scanning laser ophthalmoscopy (cSLO)

Confocal Scanning Laser Ophthalmoscopy (cSLO) is a retinal fundus imaging system. It is similar to the standard scanning laser microscope with the difference that in cSLO imaging the optics of the eye function as the objective/condenser lens. cSLO uses a confocal aperture in front of the detector to ensure that the out of focus light is suppressed for better image contrast compared to the traditional fundus imaging [72]. cSLO scans a rectangular pattern of parallel lines with a low power laser beam by utilizing horizontal and vertical scanning mirrors and create a focused raster image. The intensity of the cSLO image represents the amount of reflected light obtained in a time sequence, from a single wavelength. The reflected light intensity is registered by a detector and a 2D image is generated [72]. Aside from acquiring normal reflectance images, SLO can be used for other retinal imaging modalities such as fundus autofluorescence (FAF), fluorescein angiography (FA) and indocyanine green (ICG) angiography (ICGA). cSLO records and averages series of single images to reduce background noise and enhance image contrast. FAF imaging can be performed within seconds at low excitation energy, below the maximum retinal irradiation limits, due to cSLO high sensitivity and high frame rate. In this study, we used a commercially available cSLO system (Heidelberg Retina Angiography (HRA) Spectralis; Heidelberg Engineering, Germany) is combined with Optical Coherence Tomography (OCT).

1.5.2. Optical coherence tomography (OCT)

OCT is a non-invasive imaging modality widely used by ophthalmologists to examine the structure of the retinal layers including neurosensory retina, retinal pigmented epithelium (RPE), Bruch's membrane, and choroid with an axial resolution of several microns [73]. OCT has a similar principle to ultrasound but uses light instead of sound waves. The beam of light is directed onto the tissue and the echo time and intensity of the backscattered light from different tissue structures at varying axial distance in the eye are measured. Backscatters are caused by differences in refractive index in the transition from one tissue to another. The backscatter from the deeper tissue can be differentiated from the more superficial tissue as the light from deeper tissue takes longer to reach the sensor compared to the superficial tissue. With OCT imaging of the retina, the time difference between the backscatter signal reaching the sensor from the innermost layer and the outer most layer is very small [74]. This is because OCT uses light which has much faster speed compared to sound for imaging only 300-500μm retinal tissue. Interferometry is used to measure the time difference. Lights reflected off the tissue surface are then detected and interfered, providing anatomical information about the tissue depth [75]. There are two types of OCT imaging: Time-Domain OCT (TD-OCT) and Spectral-Domain OCT (SD-OCT). In the TD-OCT the reference arm is moving back and forth to match the delay in various layers of the sample which increases the imaging acquisition time. TD-OCT also uses a single detector to detect the signal output from the interferometer and then process and display the image on the computer screen. It has a fixed reference mirror, which is decreases image acquisition time. In SD-OCT, the interference between the subject and reference reflection is split into a spectrum and

captured by a spectrometer instead of single detector [76]. SD-OCT has faster acquisition time and higher penetration depth, and it can measure the retinal thickness from RPE to internal limiting membrane (ILM) rather than inner segment/outer segment (IS/OS) to ILM with TD-OCT [77].

Adding optical coherence tomography angiography (OCTA) to conventional OCT allowed visualization of blood flow in the retina and layers of the choroidal neovascularization in a matter of seconds. OCTA has potential application to retinal vascular diseases [78]. OCTA is non-invasive 3D imaging technique which does not require the use of contrast agent the fluorescein angiography (FA) and indocyanine green angiography (ICGA). OCTA also has higher resolution, rapid imaging, and is able to image full-thickness retina, and choroid. [78, 79].

1.6. Hyperspectral imaging

Hyperspectral imaging collects spatial and spectral information of an object, providing 3-D distribution information called the hyperspectral datacube. Chemical concentration is identified by analysis of hyperspectral datacube [80].

Hyperspectral imaging is used in the field of astronomy [81], remote sensing [82], food science [83], biotechnology and more [84]. Traditional hyperspectral imaging uses either point-scanning, line-scanning, wavelength-scanning, or compressive sampling to sequentially collect the hyperspectral datacube with temporal scanning technique [80]. Snapshot hyperspectral imager is a recent hyperspectral imaging system which collects the entire (x,y,λ) datacube simultaneously [80]. An example of such a system is the image mapping spectrometer (IMS) [85-87]. IMS captures spatial-spectral information on a single or multiple charge coupled device (CCD) image sensors in real time, which is

required for in vivo imaging. Information is provided with one to one mapping correspondence between voxels in datacube and detector pixels [80]. Some example of IMS use in the field of bioscience is to investigate cellular dynamics with multiple fluorescent biomarkers, [88] to perform real-time brain imaging [89] and for endoscopic imaging of oral mucosa [90].

1.7. Traditional medical imaging vs. non-invasive retinal imaging

Magnetic resonance imaging (MRI), and positron emission tomography (PET) are few examples of medical imaging modalities currently used to help with identifying and monitoring neurodegenerative diseases including ALS. The images generated by these modalities from inside of patient's body are used to study the structure and function of the organs. However, there are limitations associated with traditional imaging. This section discusses the limitations of traditional imaging and how retinal imaging may be more advantageous in the diagnosis and assess the disease affecting the retina.

MRI is an imaging technique used to image the soft tissue in the body. It has an imaging resolution of about 100 μm range [91]. It can help the physician to rule out the diseases such as spinal cord tumour or herniated intervertebral disk that may mimic ALS [48]. Although MRI was said to be a safe procedure with no damaging radiation like X-ray, there are several risk factors to be considered [92]. MRI uses a strong magnetic field which is 10,000-30,000 times stronger than the earth's magnetic field. Due to the strong magnetic field used in the MRI, MRI is not recommended for patients with any metal implants or fragments in their bodies as well as pregnant women due to the risk of injury and unknown effect on the fetus. Also, MRI is a costly and time-consuming imaging technique which takes about 30-60 minutes. Patients may experience discomfort going through the MRI tunnel especially those with claustrophobia. For the purpose of this project, MRI's

resolution is too low to study individual 1-micron axons,. In addition to all these limitations, the overall specificity and sensitivity of MRI imaging for the diagnosis of ALS is 76% and 48%, respectively [93].

PET uses small amounts of radioactive materials to evaluate the organ and tissue function. It can identify changes at the cellular level, and detect the early onset of disease before other imaging tests [94]. PET scanning is mostly used to detect cancer and evaluate the effectiveness of the treatment. It is also used to evaluate brain abnormalities such as memory disorder and central nervous disorders [95].

One of the limitations of MRI and PET scanning is the necessity to keep a patient in a constant position. Small head movement during acquisition may decrease the image resolution due to motion artifact [96]. This is a significant problem for the patients with limited neck mobility as seen in ALS patients with bulbar-onset. The image quality decreases when the head is not positioned in the center of the field of view where the resolution is higher. PET is resting on the detection of electromagnetic waves produced when an emitted positron and an electron annihilate. Attenuation of electromagnetic waves during their travel leads to inaccuracies in measuring the proper distribution of activity into the brain [97].

Although all these imaging techniques are used in the clinic to help with diagnosis of neurodegenerative disorders, none of them offer the resolution to study the intact nervous system at the level of single axons. In addition, PET and MRI imaging cannot show axonal pathology after injury to head [57]. As mentioned in the previous sections, the retinal pathological involvement in NDD can be imaged in a non-invasive manner using high-resolution retina-imaging techniques such as cSLO and OCT.

The eye is a much smaller organ compared to others and the retina is a very thin and transparent layer of the eye. It requires short image acquisition time with no contrast agent. The fast image acquisition minimizes motion artifact. The current retinal imaging techniques have high imaging resolution, allowing small blood vessels and axons to be detected. The laser source used for scanning is a safe, type 1 laser and there is no radioactive material, radiation or any contrast agent required during the procedure. Retinal imaging is much cheaper and repeatable compared to other neuroimaging techniques.

1.8. Eye imaging and NDD

Previous studies have suggested that pathological processes in the brain are very similar to what happens in the eye of patients with neurodegenerative diseases. Researchers have used non-invasive eye imaging to measure neuropathological features in the retina of patients with Alzheimer disease, Parkinson disease, neuromyelitis optica [98]. Retinal OCT is one of the most popular eye imaging technique used to quantify the retinal thickness in Alzheimer's disease and Parkinson's disease. OCT revealed thinning of total retinal thickness, as well as thinning of RNFL and decrease in the macular volume [99-102]. A study by Scoles and collaborators used retina fundus imaging with adaptive optics to survey in-vivo inner retinal microscopic features in retinal and neurological diseases. They identified seven categories of hyper-reflective inner retinal structures [103]. All these studies suggest retinal imaging may be used to detect and monitor the progression of certain neurodegenerative diseases in patients.

1.9. Eye imaging and ALS

Like other neurodegenerative disorders, researchers used OCT to investigate ocular biomarkers, mainly total retinal thickness, in ALS patients. While Roth and collaborators could not observe a significant difference in the RNFL thickness between ALS and control groups [33], Mukherjee and Hubers found thinner RNFL and inner nuclear layer in ALS [32, 104]. All these studies were focused on measuring global parameters such as the retinal thickness without other ocular biomarkers. Since the study was performed in vivo, no histological study of the retina tissue was performed to investigate other ocular biomarkers. In addition, OCT measurement was performed at single time point and retinal findings were not correlated with disease severity and progression.

The present research is the first study to investigate the retinal features, other than retinal thickness, in the postmortem eyes of ALS patients using OCT and cSLO imaging techniques. Since post-mortem eyes were used for this study, the histological study was also performed to further investigate the presence of the neuropathological features in the retina.

2. HYPOTHESIS AND SPECIFIC AIMS

We hypothesize that axonal pathology that occurs in the long axons of motor neurons as a result of ALS, occurs also in the retina of ALS patients, and that the axonal pathology can be detected and characterized using current eye imaging techniques. The specific aims of this study are to characterize neuropathological changes in long axons of the retinal ganglion cells in the retina sections from ALS patients and to characterize optical changes to the retina using cSLO imaging techniques, OCT, and hyperspectral imaging.

3. MATERIAL AND METHODS

Following institutional research ethics board (REB) approval, postmortem human eye specimens were obtained from the Human Eye Biobank for Research at St. Michael's Hospital and Sunnybrook Hospital. 25 eyes donated from 15 patients (age 64.93±8.33 years) clinically diagnosed with ALS and 30 age-matched control eyes donated from 18 patients (age 66.33±11.16 years) were included in this study. Tables 2 and 3 summarize clinical information of ALS and control patients, respectively. ALS mode of onset, average bulbar score, and progression of the disease are given in table 3. Exclusion criteria for age-matched controls were neurological diseases other ALS, blinding eye diseases, complicated diabetic retinopathy, and cerebral anoxia.

Table 2. Clinical information of ALS patients

** Each patient received a score from 0 (complete disability) to 4 (normal function) for speech, salivation, and swallowing. The average of these three scores is reported here.*

Case #	Gender	Age (years)	Disease Duration (Years)	Clinical Onset Duration (Years)	Mode of Onset	Average Bulbar ALSFRS-R Score*	Disease Progression
1	F	46	15.5	14.5	Non-bulbar	Unknown	Unknown
2	F	56	1.5	1.2	Non-bulbar	Unknown	Unknown
3	M	56	2	1	Non-bulbar	Unknown	Unknown
4	F	57	3	2.8	Bulbar	0	Moderate
5	F	58	2.7	0.75	Non-bulbar	1	Fast
6	M	62	6	2	Non-bulbar	2.67	Slow
7	F	66	5	2.2	Bulbar	1	Moderate
8	F	67	2.6	1.5	Bulbar	0.33	Moderate
9	M	70	18	12.7	Non-bulbar	2	Slow
10	F	71	23	15	Non-bulbar	3.67	Slow
11	F	71	9	6	Non-bulbar	Unknown	Unknown
12	M	72	3	0.42	Non-bulbar	Unknown	Unknown
13	M	73	9	7	Non-bulbar	Unknown	Unknown
14	M	74	1.1	0.7	Bulbar	0.67	Fast
15	M	75	4	2.7	Bulbar	0	Moderate

Table 3. Clinical information of control patients

Case #	Gender	Age (years)	Post-mortem time(hour) Death to Fixation	Cause of Death
1	F	43	18	Cancer
2	F	50	13	Asthma
3	F	50	16	Cancer
4	M	57	19	Cancer
5	M	59	16	Cancer
6	M	65	19	Cardiovascular accident
7	F	65	15	Pneumonia
8	M	66	24	Cancer
9	F	67	24	Liver Failure
10	M	69	1	Respiratory failure
11	M	69	22	Subdural hemorrhage
12	M	71	20	Pulmonary embolism
13	M	72	22	Hepatic cirrhosis; hepatic encephalopathy
14	F	73	18	Chronic obstructive pulmonary disease
15	F	74	17	Cancer
16	M	75	39	Cancer
17	F	77	24	Myocardial infarction
18	M	92	16	Myelodysplastic syndrome

Ten pairs of postmortem ALS eyes were imaged with Spectralis HRA+OCT scanning laser ophthalmoscope followed by histology sectioning and staining using hematoxylin and eosin (H&E), Periodic acid-Schiff (PAS) staining and immunofluorescence staining. Five eyes from 5 ALS patients were used for retina flat-mount and immunofluorescence staining. Sixteen age-matched control eyes from 8 patients were also imaged with Spectralis HRA+OCT - cSLO. Ten eyes from 10 patients were sectioned and stained with H&E and PAS. Five eyes from 4 control patients were not available for imaging with Spectralis and only retinal sections were used for tissue histology (H&E, PAS, and

immunofluorescence). Five eyes from 5 control patients were used for retina flat-mount and immunofluorescence staining. Table 4 shows imaging and staining used for each eye.

Table 4. Staining methods and eye imaging used for each eye in ALS and control groups

Control Case #	1	2	3	4	5	6	7	8	9	10	11	12	13	14	15	16	17	18
PAS/H&E staining (Retina section)		*				*	*		*	*	*			*		*	*	*
Immunofluorescence (retina section)		*				*	*		*	*	*			*		*	*	*
Whole Globe cSLO/OCT imaging			*	*	*		*			*		*	*					*
Immunofluorescence (retina flat-mount)	*				*			*					*		*			
ALS Case #	**1**	**2**	**3**	**4**	**5**	**6**	**7**	**8**	**9**	**10**	**11**	**12**	**13**	**14**	**15**			
PAS/H&E staining (Retina section)	*			*	*	*	*	*	*	*				*	*			
Immunofluorescence (retina section)	*			*	*	*	*	*	*	*				*	*			
Whole Globe cSLO/OCT imaging	*			*	*	*	*	*	*	*				*	*			
Immunofluorescence (retina flat-mount)		*	*								*	*	*					

3.1. Postmortem tissue preparation

All eyes were immersion-fixed in 10% formalin within 40 hours of the patient's

death. Then, eye specimens were washed with cool running tap water for 8 hours and were stored in 60% alcohol at room temperature.

3.1.1. Whole globe

Prior to cutting the globe, the specimens were oriented based on a few landmarks. The insertion of the inferior oblique muscle on the globe, located at the back of the sclera and temporal to the optic nerve, was used as the first landmark whenever possible. To confirm this finding, the sclera curvature was checked. The nasal sclera is flatter with a lesser radius of curvature than the temporal sclera, making the cornea to be pointed nasally. Once temporal and nasal sides of the eyes were identified, the 12 o'clock position was marked with a red pencil on the posterior sclera. The nasal or inferior cap of each eye was cut with the surgical blade (# 22, Fisher Scientific, Markham, Canada). An oblique cut was made about 2 mm away from the nasal side of the optic nerve through the iris. Eyes were split into the nasal cap and temporal cap with optic nerve head and macula. Figure 5 shows a right eye after the sectioning of the nasal cap.

Figure 5. Whole globe cut into the nasal calotte and temporal piece

Whole globe being cut into nasal cap (smaller piece) and the temporal cap (larger piece) with the lens, optic nerve and the macula. In the figure, N stands for nasal and T for temporal.

Although removing the nasal cap was preferred over the inferior cap, as it helps to image the fundus in the same positioning as in-vivo eye imaging, we had 8 ALS eyes from 8 different patients which their inferior cap was sectioned and removed. Each piece of the eye was placed in the plastic mold (Peel-A-Way, Disposable plastic tissue embedding mold, Location) and mounted by 1.5 % agar (Sigma-Aldrich, Oakville, Canada) solution prepared using milli-Q water (Millipore, Etobicoke, Canada). The nasal cap was stabilized by pouring 1.5% agar solution 2/3 the depth of the plastic mold and placing the nasal piece with the outer surface of sclera facing down on the top of semi-solid agar. The temporal cap was placed on one end with sclera facing the agar, iris down and optic nerve up (Figure6).

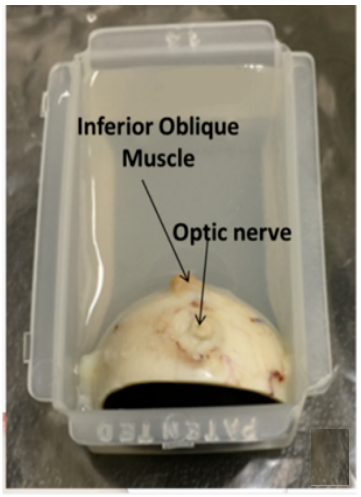

Figure 6. Agar embedded eye preparation for retinal imaging.

Temporal cap of a right eye stabilized in 1.5% agar mould, prepared for imaging with cSLO and OCT modes of Spectralis imaging system.

3.1.2. Retina flat-mount

Eyes were cut in the same way as for whole globe imaging. Only the retinal tissue from the nasal cap was used for the retina flat-mount staining and imaging. Dissection of the retina from the nasal cap was performed in a petri dish, with 1xPBS covering the surface of the dish to prevent dehydration of the tissue [105]. Two small pieces of (approximately 1 cm^2,) peripheral or mid-peripheral retina from the nasal cap were dissected using tweezers and small scissors for imaging before staining, each retina piece was flat-mounted on a microscope slide with inner surface up. The mounting of the tissue was performed under a dissecting microscope (Zeiss, Toronto, Canada) to ensure the retinal tissue was flat with minimal folds. The tissue was mounted with PBS and covered with #1.5 coverslip. Once pre-staining imaging was completed with Spectralis cSLO and OCT, the tissue was removed from the slides for immunofluorescence staining. One flat-mount piece from each eye was stained with mouse anti-neurofilament H phosphorylated antibody (SMI31, BioLegend, San Diego, CA), and the second piece was used as negative control, with the primary antibody omitted. All flat-mounted tissues were stained with the secondary antibody, CF770 dye-conjugated goat anti-mouse IgG (Biotium, Fremont, CA). Detailed information about the immunofluorescence staining is provided in section 3.2.3.

After the staining, the retinal tissue was mounted with 1xPBS on the microscope slide, with inner retinal surface up, and covered with #1.5 coverslip for cSLO and OCT imaging. 1xPBs was constantly added between the microscope slide and coverslip to prevent tissue from drying up during the imaging session. After the imaging, the tissue was mounted with Dako Fluorescent Mounting Medium (Dako, North America, Inc.,

Carpinteria, CA) to preserve the tissue. Mounted slides were allowed to dry overnight under the fume hood, shielded from any light source. The slides were then stored at 4 °C in a refrigerator and covered with aluminum foil for future use.

3.1.3. Retina sections

For histopathology study, the eyes were placed in steel mesh cassettes and were processed in the Pathology lab of the St. Michael's Hospital. The eye specimens were dehydrated in graded alcohols (70% to 100%) then cleared in xylene, infiltrated and embedded in paraffin. Paraffin-embedded tissue blocks were cut at 8 μm thickness using rotary microtome (AO Spencer #820), then placed on the microscope slides (Thermo Fisher Scientific, Mississauga, Canada).

3.2. Staining

3.2.1. H&E and PAS staining of retina sections

Eight μm sections mounted on microscope slides were stained with Hematoxylin and Eosin (H&E) and Periodic acid–Schiff (PAS) stains. Sections were scanned with an Aperio AT Turbo scanner (Leica Biosystems, GmbH, Nussloch, Germany) at 20x magnification.

3.2.2. Immunofluorescence staining of retina sections

For immunofluorescence staining of the paraffin-embedded sections, sections were deparaffinised and rehydrated using a Leica Autostainer XL (Leica Biosystems, Nussloch, Germany). Sections were heated at 65˚C for ten minutes and then underwent

one three-minute wash in xylene, two two-minute washes in xylene, two one-minute washes in 100% alcohol, and one one-minute wash in 95% alcohol. Heat-induced epitope retrieval was achieved using a Biocare Medical Decloaking Chamber™ (Biocare Medical, LLC, Concord, CA). Sections were placed in a staining dish filled with 10mM citric acid, pH 6, and the dish was immersed in 500mL distilled water in the chamber. Sections were heated at 95˚C for 20 minutes, followed by 90˚C for ten seconds. Sections were then allowed to cool on the benchtop for 20 minutes immersed in phosphate-buffered saline (PBS). Sections were rinsed twice in PBS, five minutes each, and then incubated in blocking solution (2% goat serum, 0.3% TritonX-100 in PBS) for 40 minutes at room temperature. Incubations in primary antibodies (diluted in blocking solution) were carried out overnight at 4˚C. Sections were stained with anti-P-NF (SMI 31, mouse monoclonal, 1:500; BioLegend, San Diego, CA). Negative controls without primary antibody were processed in parallel. Sections were then rinsed three times in PBS, five minutes each. Sections were incubated in Alexa-Fluor 555 goat anti-mouse IgG (H+L) (1:1000; Invitrogen cat. A31570) and 4',6'-diamino-2-phenylindole (DAPI, 1:1000; Thermo Fisher Scientific, Waltham, MA) for one hour at room temperature, protected from light. Sections were then rinsed three times in PBS, five minutes each, and coverslips were mounted using Dako Fluorescent Mounting Medium (Dako, North America, Inc., Carpinteria, CA) [106]. Slides were dried for two hours in the fume hood, protected from light, and were then stored at 4˚C overnight. The sections were imaged using a Zeiss LSM 700 confocal scanning laser microscope (Carl Zeiss MicroImaging, Ltd., Göttingen, Germany). Images of the central and peripheral retina and at the optic nerve head were captured. Images were analyzed in a masked manner.

3.2.3. Immunofluorescence staining of retina flat-mount

Flat-mounted tissues from ALS and control retina were immunofluorescence stained for phosphorylated neurofilament. Before staining, they were incubated in 0.2% Triton X-100 (Sigma-Aldrich Canada, Co., Oakville, ON) for 36 hours at room temperature (RT). The solution was replaced 3 times at 12-hour intervals. Once pre-treatment was complete, the tissue was transferred to the blocking solution (5% goat serum, 0.5% Triton X-100) for 2 hours at RT. Afterward, the tissue was incubated in diluted primary antibody solutions at 4˚C for 48 hours. The primary antibody used for retina flat-mount was anti-phosphorylated neurofilament H antibody (SMI 31, mouse monoclonal, 1:200 dilutions, BioLegend, San Diego, CA). Tissues without primary antibody were processed in parallel as a negative control. After primary incubation with primary antibody, the tissue was incubated in a solution of CF770 dye-conjugated secondary antibody (goat anti-mouse IgG, 1:200 dilutions, Biotium, Fremont, CA) and 4',6'-diamino-2-phenylindole (DAPI, 1:1000 dilution; Thermo Fisher Scientific, Waltham, MA). The tissue was then rinsed six times, 10 minutes each, with 1xPBS at RT [107]. Once the washes were complete, the tissue was mounted on microscope slides (Thermo Fisher Scientific, Mississauga, Canada) with 1xPBS for imaging with Spectralis. After imaging, tissue was mounted with Dako Fluorescent Mounting Medium (Dako, North America, Inc., Carpinteria, CA) and covered with #1.5 coverslips (Thermo Fisher Scientific, Mississauga, Canada) for longer preservation of the tissue. Tissue where then stored at dark in a refrigerator with 4˚C for future use.

3.2.4. Confocal images of immunofluorescence stained retina sections

P-NF immunoreactivity in RGC axons was quantified using Fiji image processing software. For each eye, several regions from peripheral to central RNFL and optic nerve head was selected and the mean pixel intensities within those regions were calculated. For statistical analysis, the eye with higher mean pixel intensity was selected and compared between ALS and control patients using a two-sample t-test ($\alpha = 0.05$). A correlation between P-NF immunoreactivity and the patient's clinical characteristics was assessed. In addition, a linear regression model was used to test the effects of age, disease duration, and clinical severity of disease on mean pixel intensity. A two-sample t-test was used to compare patients with bulbar onset disease to those with non-bulbar onset. A single-factor ANOVA was used to test the effect of the rate of disease progression on mean pixel intensity. A significance level of 0.05 was used in all tests.

3.3. Eye imaging

3.3.1. cSLO and OCT imaging of the whole globe

Retina fundus and cross-section images of whole eye globes were imaged with Spectralis HRA+OCT. The agar-embedded specimen was mounted on a flat platform. A set of +25 diopter (+25D) lens was mounted on the camera objective of the Spectralis to enhance the focusing power (Image 3). The Spectralis was used to capture reflectance and fluorescence images with the following acquisition modalities, namely Infrared Reflectance (IR), Blue Reflectance (BR), Infrared Autofluorescence (IRAF), and Blue Autofluorescence (BAF). Parallel beam, class 1 laser product was used for all acquisition

modes with varying wavelengths (see Table 5). In addition, retina fundus and cross-section images were taken simultaneously, side-by-side with the cSLO+OCT mode. Super luminescence diode was used as a light source for spectral-domain OCT with an average wavelength of 870 nm.

Table 5. Imaging modes of Spectralis HRA+OCT

	Imaging Modes	**Laser Wavelengths**	**long-pass Fluorescence Filter**
Reflectance	Blue Reflectance (BR)	486 nm	500 nm
	Infrared Reflectance (IR)	815 nm	N/A
	Multicolour Reflectance (MColour: Simultaneous Blue Reflectance, Green Reflectance, and Infrared Reflectance)	486 nm, 486 nm, 815 nm	N/A
Angiography	Blue Autofluorescence (BAF)	486 nm	N/A
	Infrared Autofluorescence (IRAF)	786 nm	830 nm

The specimen was placed on the platform with the cut surface facing the camera, and the side of the mold covering the cut surface was removed. The retina faced the camera (Figure 7). The temporal and nasal caps of the eye were first imaged using the two reflectance modes, BR and IR. Afterward, IRAF and BAF images were acquired with the Angiography acquisition mode at a different angle from the eye. All cSLO images of the globes were taken as ART (Automatic Real Time) Mean images with a frame count up to

100. Hyper-reflective profiles were seen in cSLO and OCT images of the retina. For image quantification (section 3.4), unbiased Stereo Investigator software (MBF Bioscience, Inc., Williston, VT) was used in a masked fashion and student t-test was used for statistical analysis to compare ALS and control groups.

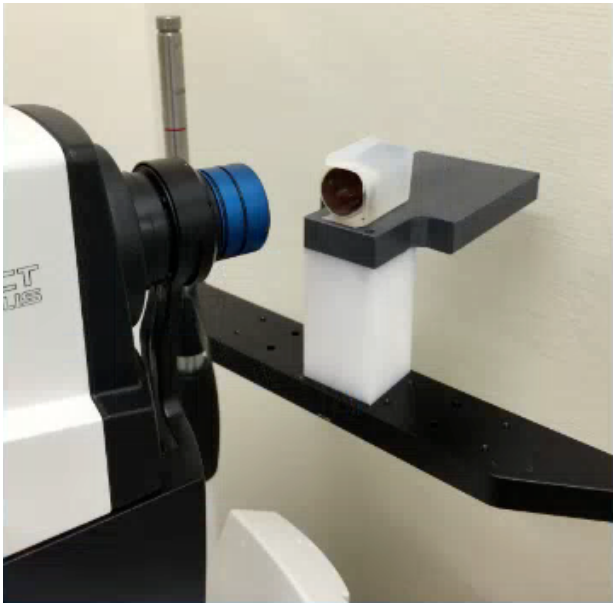

Figure 7: Set-up for cSLO and OCT imaging of whole globe.

A +25D lens (blue colour) mounted on Spectralis HRA+OCT. The specimen is placed in front of the lens on the gray custom made stage.

Optical Coherence Tomography (OCT) was performed while the device was set on the reflectance module with the +25D lens mounted. When the OCT mode was activated, the 15-degree single line scan was selected and placed at different locations over the fundus retina image. Retina cross-section images were captured with a frame count up to 100. cSLO and OCT images were taken simultaneously and were viewed side by side in the picture. The wavelength of the light source for OCT imaging was 870 nm. OCT images were used to confirm the presence of the profiles observed by the cSLO images.

3.3.2. cSLO and OCT imaging of retina flat-mount

Spectralis HRA-OCT was used to capture images of flat-mounted retinal tissue before and after immunofluorescence staining. The microscope slide was placed on a slide holder in front of the camera. Two sets of lenses, +25D and +90D, were used to enhance focus. Microscope slides were positioned differently when imaging with the two lenses. With the +25D lens, the slides were mounted on the slide holder. With the +90D lens, they were taped onto the front surface of the slide holder to shorten the distance between the lens and the tissue. The flat-mount retina was imaged with IR, BR, IRAF and BAF modalities. Automatic Real-Time (ART) Mean images were taken with up to 100 frames to image with an optimal contrast. Three sets of images were taken, both before and after immunostaining. Flat-mount retina images with the +25D lens at 30° Scanning Angle as well as a +90D lens at 30° scanning angle were captured. Images of two selected regions of interest (ROIs) per tissue were captured with the +90D lens at 15° scanning angle. All four modalities were used in each set of the images. The two ROIs were selected before staining at areas with visible hyper-reflective profiles under the BR mode. Images were taken at the same locations after-staining. The position and focus of the camera were adjusted to attain the best resolution in the BR mode before staining and IRAF mode after staining. Once focus was adjusted, the camera position was maintained image acquisitions with all four modalities. In addition to cSLO images, OCT images were obtained from the tissue. The same +25D and +90D lens for capturing cSLO images were used for OCT. Positions of the slides were also the same for OCT and cSLO imaging for the two lenses. Before staining, OCT images were captured along sections of the tissue with visible hyper-reflective profiles in either IR or BR modes before staining.

After staining, OCT images were captured along the same sections whether those hyper-reflective profiles were still visible or not. In addition, simultaneous IRAF+OCT images were captured along sections with visible hyper-reflective profiles. However, it was not always possible to attain OCT images when using the +90D lens. If +90D OCT images were unavailable, +25D OCT images of those locations would be taken instead.

3.3.3. IMS imaging of retinal flat-mount

Custom-made snapshot Image Mapping Spectrometer (IMS) was used to capture images of immunofluorescence stained, flat-mounted retinal tissue after imaging with cSLO and OCT. This equipment was driven by Reveal Hyper software (Reveal Hyper; Modular Light, Inc., Tucson, AZ). IMS images were taken under the fluorescence mode. The xenon lamp (LB-LS/OF30IR model with 380LLG (Liquid Light Guide) (Sutter Instrument, Novato, USA), with wavelengths ranging between 375nm and 925nm, was turned on at least for one hour before imaging to reach its optimal temperature. A microscope slide coated with CF770 dye-conjugated goat anti-mouse IgG and Dako Fluorescent Mounting Medium, covered with a #1.5 coverslip was placed on the stage of the microscope with the Near Infrared Fluorescence (NIRF) filter applied. The NIRF filter allowed excitation with near-infrared light at a wavelength of 780 nm and higher to pass through. Before capturing any images of the tissue, the flat-field correction was performed to correct the variation in pixel-to-pixel sensitivity due to the image split by sets of tilted mirror facets. The flat-field correction, a flat-field corrected image, and a dark noise flat-field image were taken. Dark noise images were taken by blocking the pathway of light entering the IMS. Afterward, the slides with flat-mounted retinal tissue

were placed on the microscope stage. After the focus was adjusted, a custom-made script in MATLAB was used to capture images of the selected ROI. Three images were taken per location with an overlap of 12% between each location. The overlap allowed more accurate tiling for the final Mosaic image. A dark noise sample image was saved after the images of the tissue were taken. The images were then stacked and stitched up by ENVI and IDL image processing software (Harris Geospatial Solution, Broomfield, CO, USA). A mosaic image capturing the whole ROI was compiled for each tissue.

3.4. Quantification and data analysis

3.4.1. cSLO-BR images of the whole globe

The Stereo Investigator (MBF Bioscience, Inc., Williston, VT) software was used to quantify the hyper-reflective profiles observed in the BR images of the whole eye, captured by the Spectralis HRA-OCT. Before any analysis, the image scale was calculated with image processing software (Fiji, Madison, USA). First, the cSLO images were opened and magnified in Fiji software. The magnification was done so that the edges of the scale bar provided in the cSLO image would be visibly differentiable from the image surrounding it. A straight line was drawn along the scale bar between the start and end edges of the actual distance. It corresponds to the length of the line, stated under the scale bar in the cSLO image. The scale of the image, in pixel/micron, was calculated. The number was recorded and inversed for later use. Afterward, the same cSLO images were opened with Stereo Investigator. The inversed number recorded from Fiji, in micron/pixel, was set as the scale of the image for both the x- and y-axis. An ROI was selected by drawing the largest possible square on the tissue where the image was

focused, with the guide of a grid displayed on the screen. The hyper-reflective profiles in this selected area would be calculated in the following manner. First, the ROI was divided into smaller fractions, each with a size of 500 by 500 micron. In each fraction, the profiles within one counting frame, each with a size of 250 by 250 micron, would be marked and recorded. Note that the top left counting frame in each fraction was used. Profiles located within the counting frame, directly on the top or the right borders were all taken into account. Once the measurements were complete, the numbers of profiles in these counting frames were totaled for all fractions in the ROI. Since the profiles in the only ¼ of the area in each fraction were quantified, Stereo Investigator would estimate the number of profiles within the whole ROI selected. The density of these profiles on the tissue was calculated by dividing the total estimated number of profiles by the area of the ROI.

For statistical analysis, the natural logarithm of profile density counted from each eye in every group was calculated to convert the profile density data to normal distribution dataset. A student t-test with $\alpha = 0.05$ was used to test for statistically significant difference in profile density between two groups. A linear regression model was built to determine the impact of disease duration and the clinical onset duration on hyper-reflective profiles density.

4. RESULTS

4.1. Histopathology of retina sections

4.1.1. PAS staining

Round profiles of 3-25 μm in diameter were found scattered across the RNFL and RGC layer. These round structures were reddish-purple and were enclosed by a narrow band in a darker shade of purple (Figure 8). PAS-positive profiles were found in all of 10 ALS patients and only 4 out of 10 control patients.

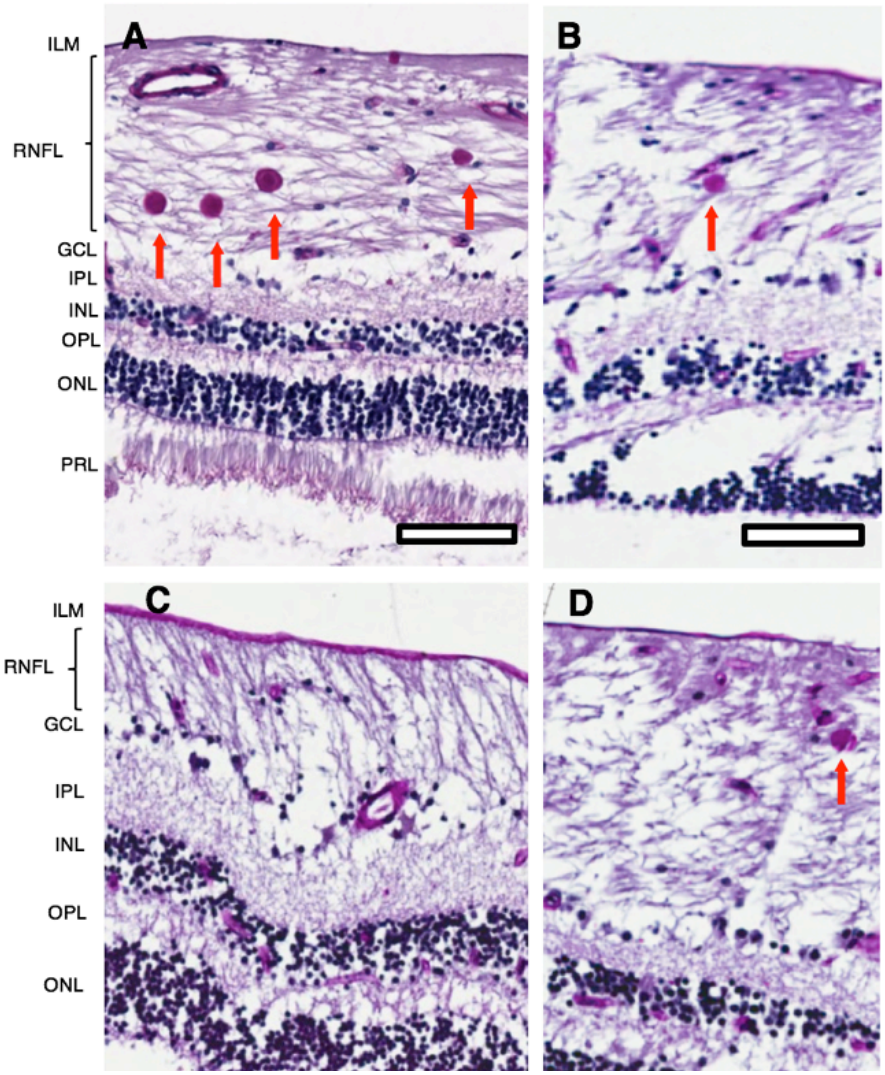

Figure 8. PAS-stained sections revealed round profiles in the RNFL

(A)-(B) PAS stained ALS retina sections showing purple round profiles (red arrows) in the RNFL.
(A) 62 y/o male; (B) 67 y/o female

(C)-(D) PAS stained control retina sectins. Only few control patients showed purple round profiles in the RNFL. (C) 73 y/o female; (D) 75 y/o male.

Abbreviations: ILM = internal limiting membrane; RNFL = retinal nerve fiber layer; GCL = ganglion cell layer; IPL = inner plexiform layer; INL = inner nuclear layer;
OPL = outer plexiform layer; ONL = outer nuclear layer; PRL = photoreceptor layer.

Scale bar = 100μm.

H&E stained adjacent retina sections showed grayish-purple color profiles with similar morphology observed in PAS, also in RNFL (Figure 9).

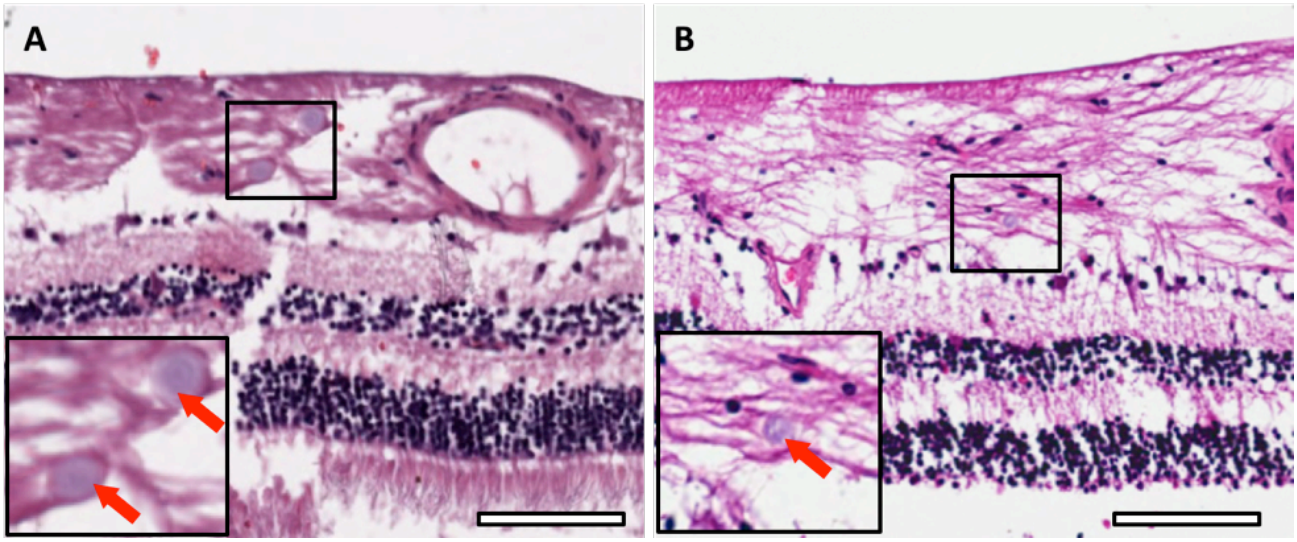

Figure 9. H&E stained retina sections revealed round profiles in the RNFL.

(A) H&E-stained retina section of a 62 years old male ALS patient and (B) 73 years old control female patient showing round profiles in the RNFL. Profiles are stained grayish-purple with H&E.

Scale bar = 100μm.

These profiles were predominantly observed in the RNFL and occasionally between the nerve fibers in the optic disc and within the optic nerve fiber bundles. Figure 10 shows these profiles in the peripapillary retina, in PAS and H&E stained sections.

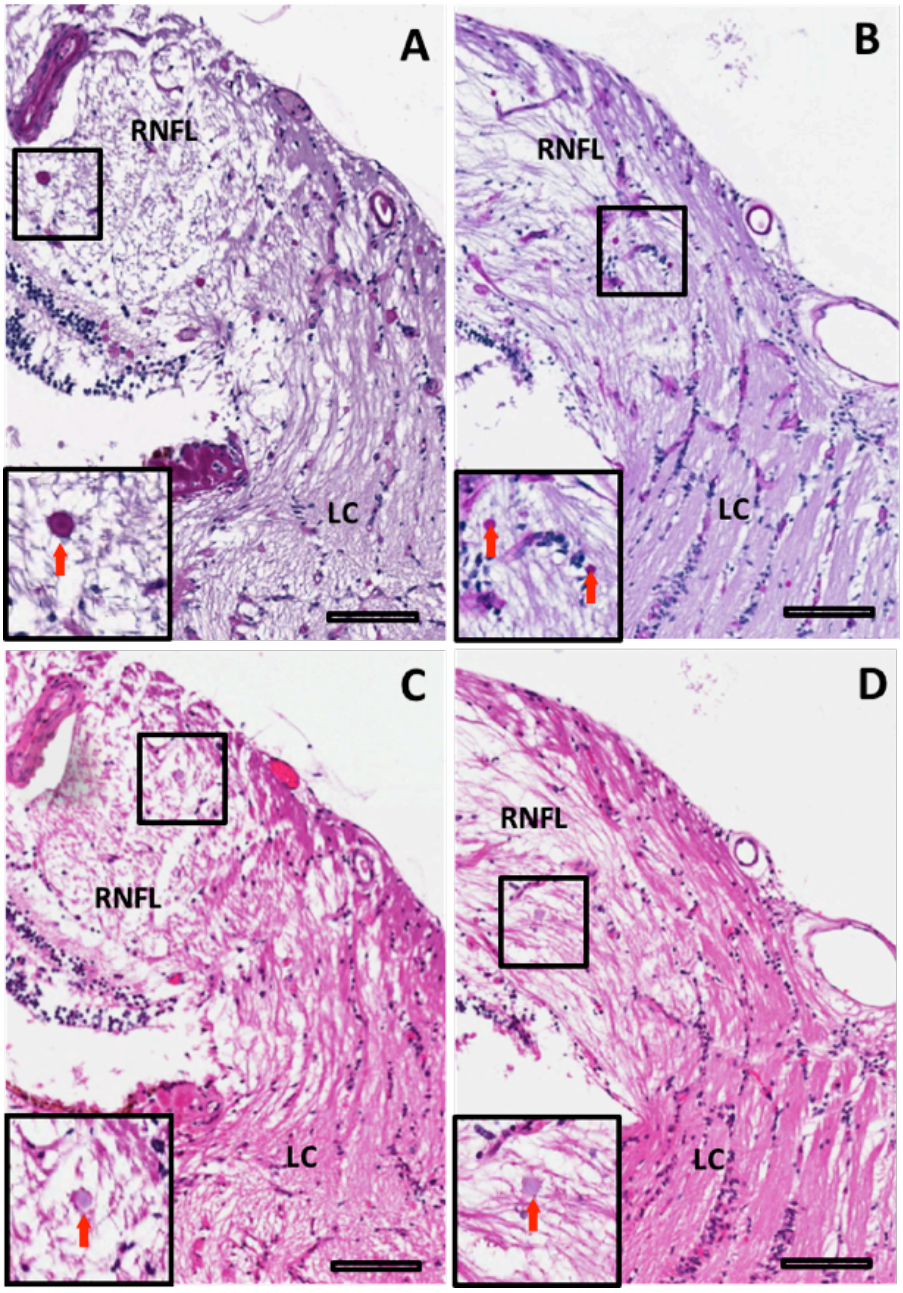

Figure 10. PAS and H&E stained sections revealed round profiles in the central RNFL of ALS patients

(A)-(B) PAS-stained of retina section around the optic nerve head of ALS patients revealed round profiles (shown with red arrows) in the peripapillary RNFL. (A) 62 y/o male; (B) 57 y/o female.

H&E stained sections from the same patients in panels A and B showed similar profiles in grayish-purple colour pointed with red arrow.

Abbreviations: LC = lamina cribrosa; RNFL = retinal nerve fiber layer.

Scale bar = 100μm.

4.1.2. Immunofluorescence staining

Immunofluorescence staining of all ALS retina sections revealed the accumulation of P-NF in the axonal processes of RGCs in the retinal nerve fiber layer. Three to four P-NF positive round profiles, 8-15μm in diameter, were observed in each of the ALS retina sections. These structures were found in the central RNFL for all ALS patients and peripheral RNFL of 7 out of 10 patients. Only 1 out of 10 control patients had these profiles detected in the central RNFL (Figure 11).

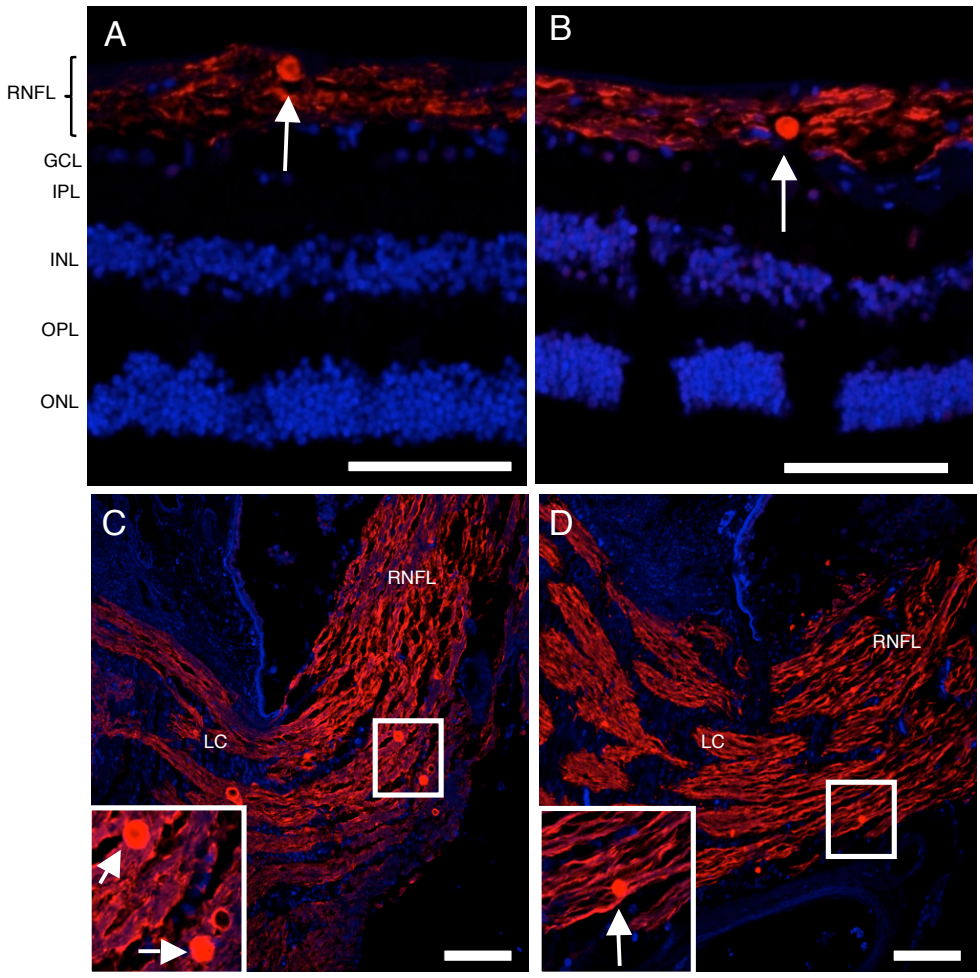

Figure 11. Immunofluorescence staining for P-NF (SMI 31) showed round SMI31 positive profiles in the RNFL of ALS retina.

All panels are from ALS patients. Sections show SMI 31 (P-NF) immunostaining in red and DAPI counterstaining in blue. SMI 31+ round profiles, 8-15µm in diameter, are indicated with white arrows

(A)-(B) round profiles were observed in the peripheral RNFL. (A) = 70 y/o male; (B) = 67 y/o female.

(C)-(D) round profiles were observed in central RNFL. (C) = 62 y/o male; (D) = 71 y/o female.

Abbreviations: RNFL = retinal nerve fiber layer; GCL = ganglion cell layer; IPL = inner plexiform layer; INL = inner nuclear layer; OPL = outer plexiform layer; ONL = outer nuclear layer; LC = lamina cribrosa.

Scale bar = 100µm

Mean pixel intensity of SMI31, stained with red for P-NF, in RGC axons was significantly larger in ALS patients compared to controls (figure 12-13) with 16777.3 ± 2904.1 vs. 353.9 ± 2053.4 (Mean ± SD; $p < 0.001$). A linear regression test with p-value > 0.05 determined no significant correlation between disease duration and clinical onset duration, with mean pixel intensity of P-NF immunoreactivity.

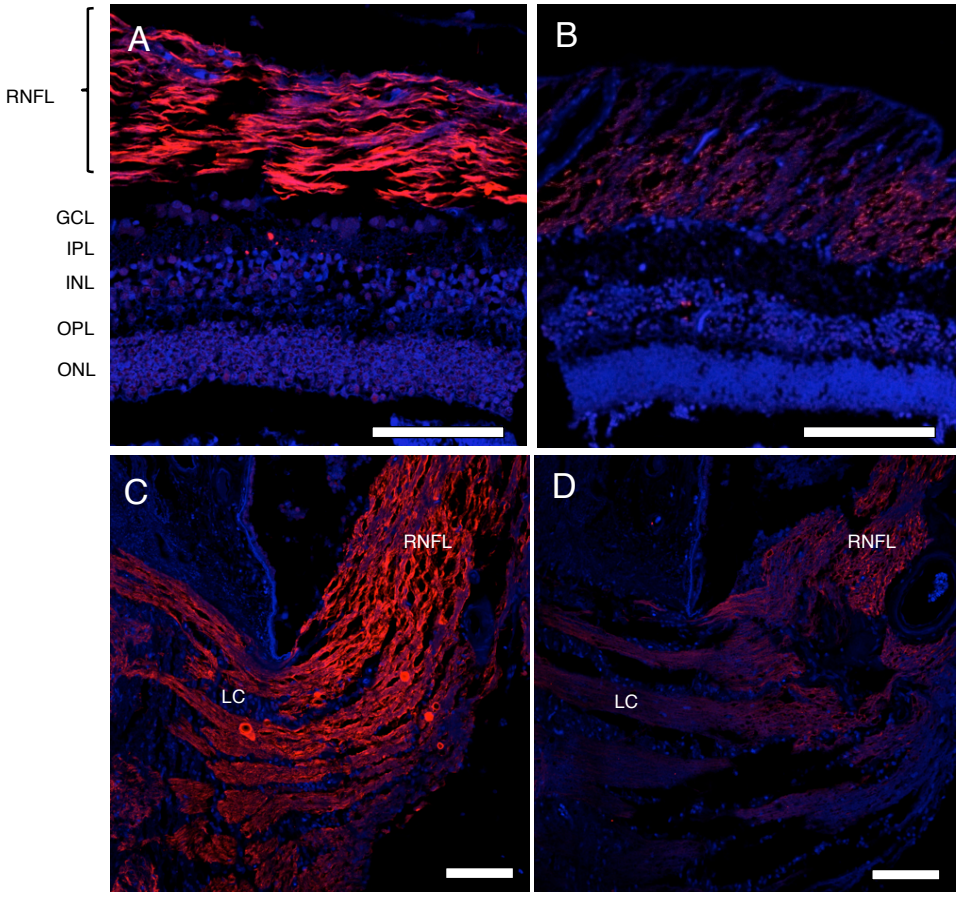

Figure 12. P-NF Immunofluorescence staining of (SMI 31) in the retina showed increased P-NF immunoreactivity in ALS patients compared to controls

All panels show SMI 31 (P-NF) staining in red and DAPI counterstaining in blue. Panels (A) shows increased P-NF immunoreactivity in the RNFL of ALS patient compared to panel (B) control patient. (A) = 71 y/o female; (B) = 92 y/o male.

Panel (C) is a section from central retina of an ALS patient with increased P-NF immunoreactivity compared to panel (D) a section from central retina of a control patient.
(B) = 62 y/o male; (D) = 69 y/o male.

Abbreviations: RNFL = retinal nerve fiber layer; GCL = ganglion cell layer; IPL = inner plexiform layer; INL = inner nuclear layer; OPL = outer plexiform layer; ONL = outer nuclear layer; LC = lamina cribrosa.

Scale bar = 100µm.

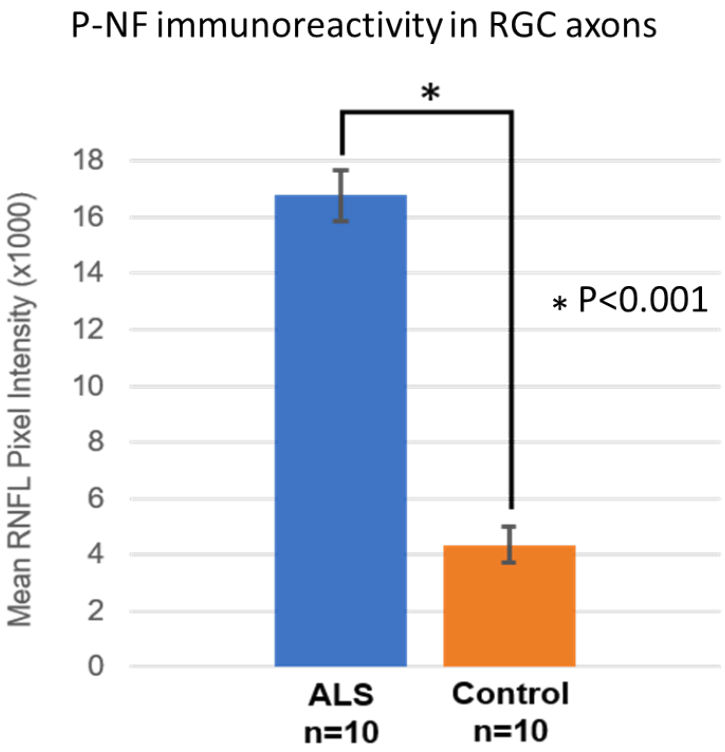

Figure 13. Graph comparing P-NF immunoreactivity in the retina sections of ALS patients vs. controls.

Statistical analysis showed significantly higher P-NF immunoreactivity in the retina sections of ALS patients (blue bar) compared to controls (orange bar) . The error bars indicate the standard errors.

4.2. Whole eye scanning

4.2.1. cSLO and OCT imaging

Hyper-reflective profiles of 10-30 μm in diameter, located on the surface of the retina, were revealed with cSLO imaging blue reflectance mode (Figure 14-15). These profiles were more frequently detected in the central regions compared to peripheral regions of the retina. More profiles were counted from each cSLO-BR images of ALS patients compared to control patients (Figure 16).

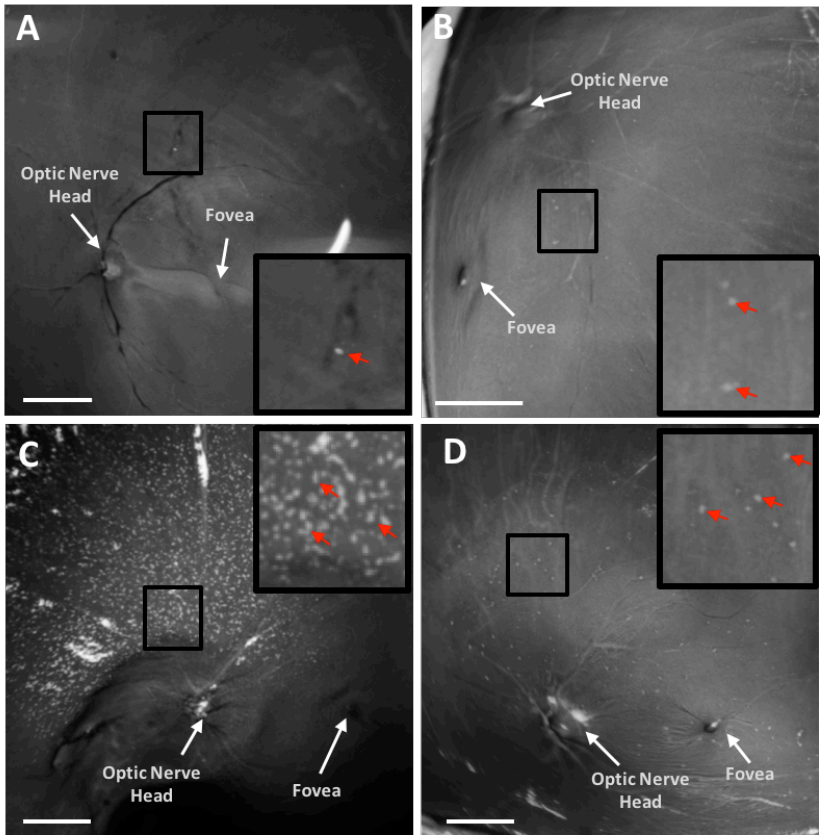

Figure 14. Hyper-reflective profiles in the retina of ALS patients

All panels show cSLO- blue reflectance images from 4 different ALS patients retina. The small black box regions are expanded and shown in the bottom right or top right corner of each Image. Red arrows indicate hyper-reflective profiles.

(A) = 62 y/o male; (B) = 59 y/o female; (C) = 74 y/o male; (D) = 67 y/o female.

Scale bar = 1.0mm

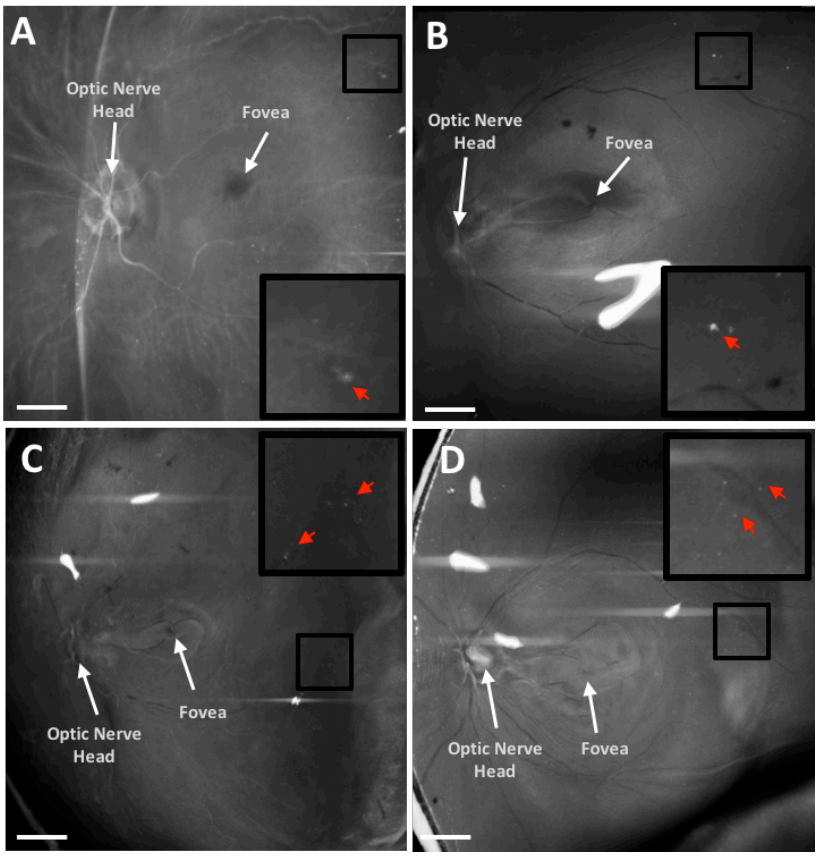

Figure 15. Hyper-reflective profiles in the retina of age-matched control patients

All panels show cSLO-blue reflectance images from 4 different control patients. The small black box regions are expanded and shown in the bottom right or top right corner of each Image. Red arrows indicate hyper-reflective profiles.

(A) = 92 y/o male; (B) = 69 y/o male; (C) = 65 y/o female; (D) = 59 y/o male.

Scale bar = 1.0mm

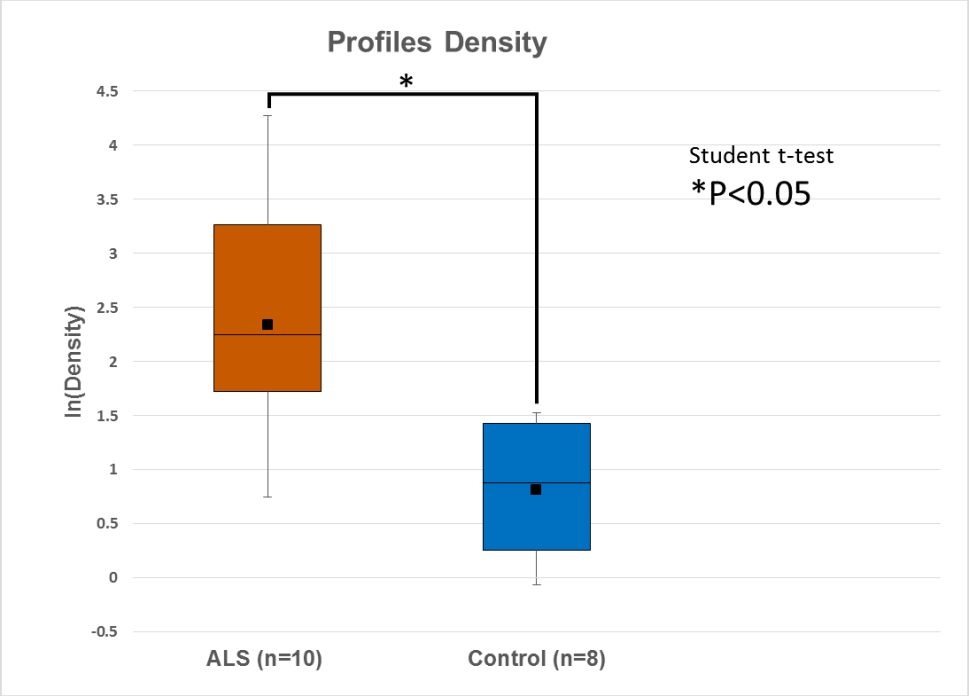

Figure 16. Graph comparing the the number of hyper-reflective profiles counted from the cSLO-BR images taken from the whole-globe retina in ALS patients compared to controls

Quantification of hyper-reflective profiles showed the mean number of hyper-reflective profiles in ALS patients (Orange box) is statistically higher than those in control patients (blue box). The graph shows the hyper-reflective profiles variations in each group of patients. The lines extending parallel from the boxes indicate variability outside the upper and lower quartiles.Tthe horizontal line through the box is the median and the small dot in the box is the mean hyper-reflective profiles.

As shown from cross-section images of the retina captured by OCT, the hyper-reflective profiles were more frequently found in the RNFL compared to other retinal layers (Figure 17).

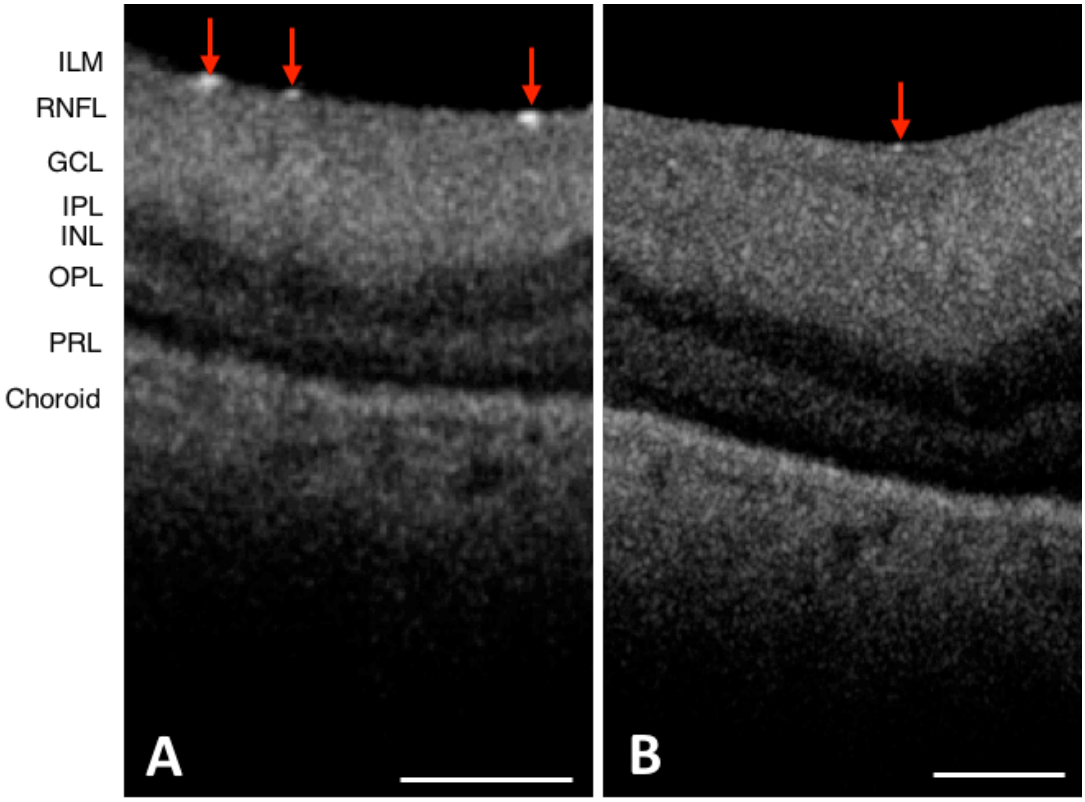

Figure 17. OCT imaging showed hyper-reflective profiles are located in RNFL

Retina cross-section image from a 67 years old female with ALS (A) and a 92 years old control male showing hyper-reflective profiles (red arrows) located in the RNFL.

Scale bar = 300 μm

A number of hyper-reflective profiles counted from cSLO-BR images is ranging from 2-5 profiles per mm^2 for controls and 3-72 profiles per mm^2 for ALS patients. Eight out of 10 ALS patients had more profiles than the maximum count per mm^2 of controls. Table 6 lists the hyper-reflective profiles density measured from cSLO-BR images of each ALS and control eye. To test for statistical significance between the profiles counted from each group the hyper-reflective profiles density data were converted to a normal distribution by taking the natural logarithm of the density values. A student t-test with $p < 0.05$ showed significantly higher hyper-reflective profiles for ALS patients than control patients. Mean profile density in control group was significantly increased in the ALS group compared to controls (19.04 ± 22.5 vs. 2.7 ± 1.6). A linear regression model was built to determine the impact of disease duration and the clinical onset duration on hyper-reflective profiles density. With a p-value larger than 0.05, there was no significant impact of disease duration and clinical onset duration on the hyper-reflective profiles. In addition, a Pearson correlation was performed between P-NF immunoreactivity and hyper-reflective profiles density. With a p-value > 0.05 there was no significant correlation between the two variables.

Table 6. Puncta distribution in ALS and control groups.

ALS case #	Profiles Density (count/mm^2)	Control case #	Profiles Density (count/mm^2)
1	3	3	2
4	11	4	2
5	6	5	5
6	3	7	5
7	34	10	1
8	11	12	2
9	9	13	4
10	7	18	5
14	72		
15	39		

4.3. Immunofluorescence staining of retina flat-mount

4.3.1. cSLO and OCT imaging

cSLO-BR images of the retina flat-mount before staining revealed the hyper-reflective profiles on the surface of the retina (Figure 18).

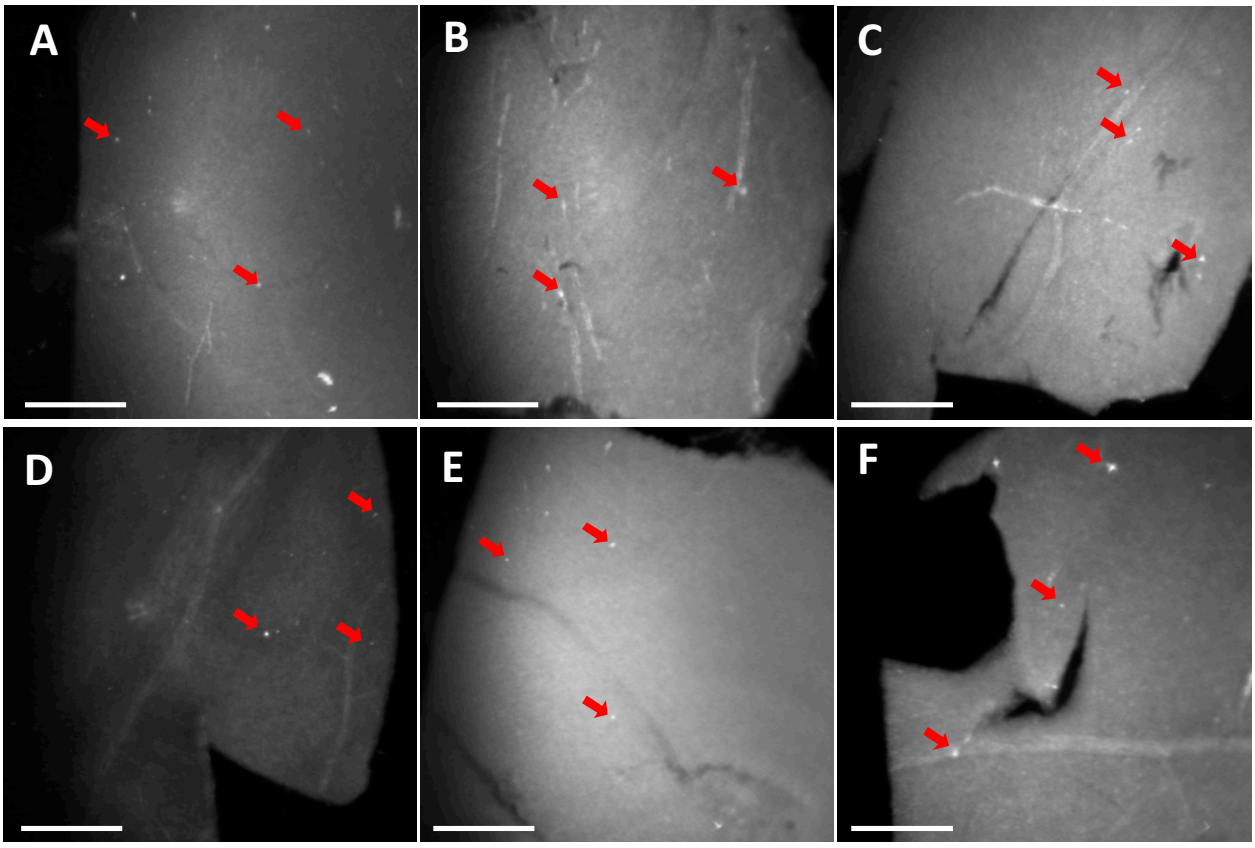

Figure 18. Hyper-reflective profiles in cSLO-BR images of retina flat-mount

All panels show cSLO-BR images. (A)-(C) are images from 3 different ALS patients. (D)-(E) are images from 3 different control patients. Red arrows in the images are pointing to the hyper-reflective profiles. (A) 72 y/o male ALS ; (B) 56 y/o male ALS; (C) 71 y/o female ALS; (D) 74 y/o female control; (E) 43 y/o female control; (F) 66 y/o male control

Scale bar = 1.0mm

Comparing cSLO-BR images before and after staining, it was not clear whether a number of hyper-reflective profiles remain the same or changes after staining (Figure 19). This was due to the false signals in the cSLO-BR images coming from dust or brush hairs trapped in the vitreous during flat-mount preparation or staining process.

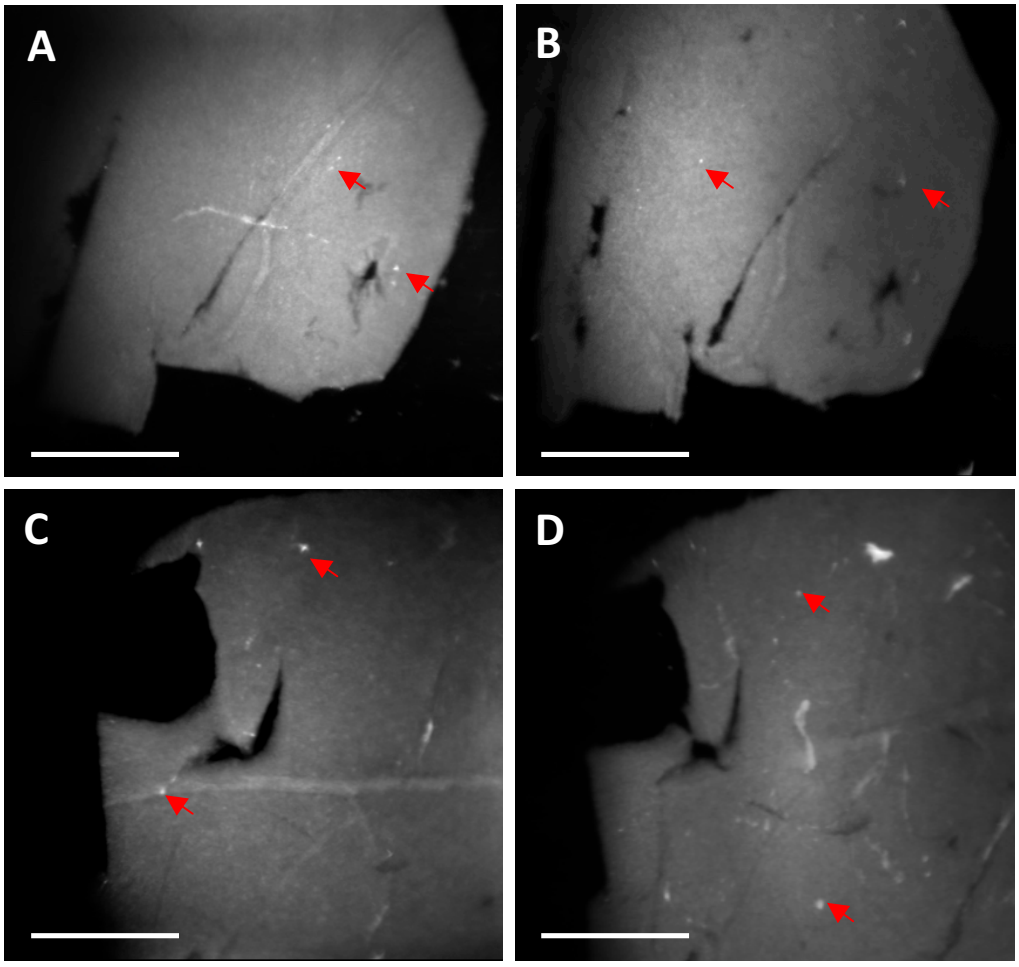

Figure 19. Hyper-reflective profiles before and after staining of retina flat-mount in cSLO-BR images

(A) ALS retina before immunostaining vs (B) after staining (71 years old ALS female). (C) control retina before staining vs (D) after staining (66 years old control male).
Images were taken with 90D lens at 15 degree scanning angle. Red arrows indicate hyper-reflective profiles.

Scale bar = 1.0mm

cSLO-IRAF images revealed no signal from all tissues before staining (Figure 20). Negative control stains were obtained by omitting the primary antibody showed effective indirect staining as indicated by the lack of NIR signal before and after staining.

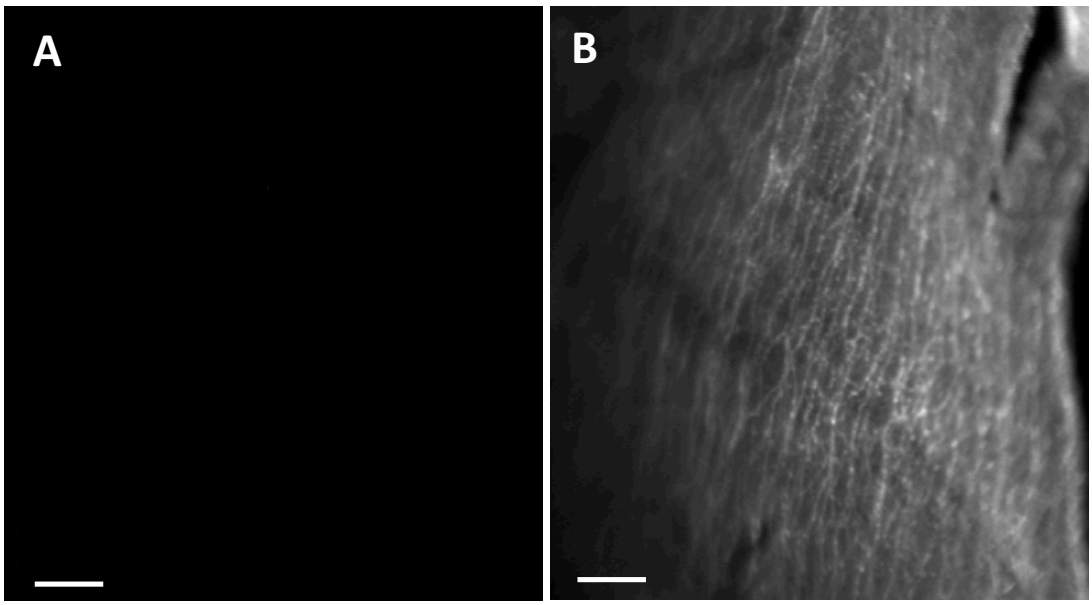

Figure 20. Successful staining of P-NF positive axons in retina flat-mount

(A) cSLO-IRAF image from the retina of a 71 years old ALS female before staining showed no NIR-fluorescence signal.

(B) same retina after P-NF fluorescence staining showed long P-NF-positive axons in the retina.

Scale bar = 200 μm

Round profiles were observed on the surface of the retina in cSLO-IRAF images after staining. OCT images were also taken to confirm whether those profiles were located in the RNFL. cSLO-IRAF images taken with 90 diopter lens at 15-degree scanning angle showed defined axonal structures extended along the retina with enlarged segments of the axons stained stronger (Figure 21).

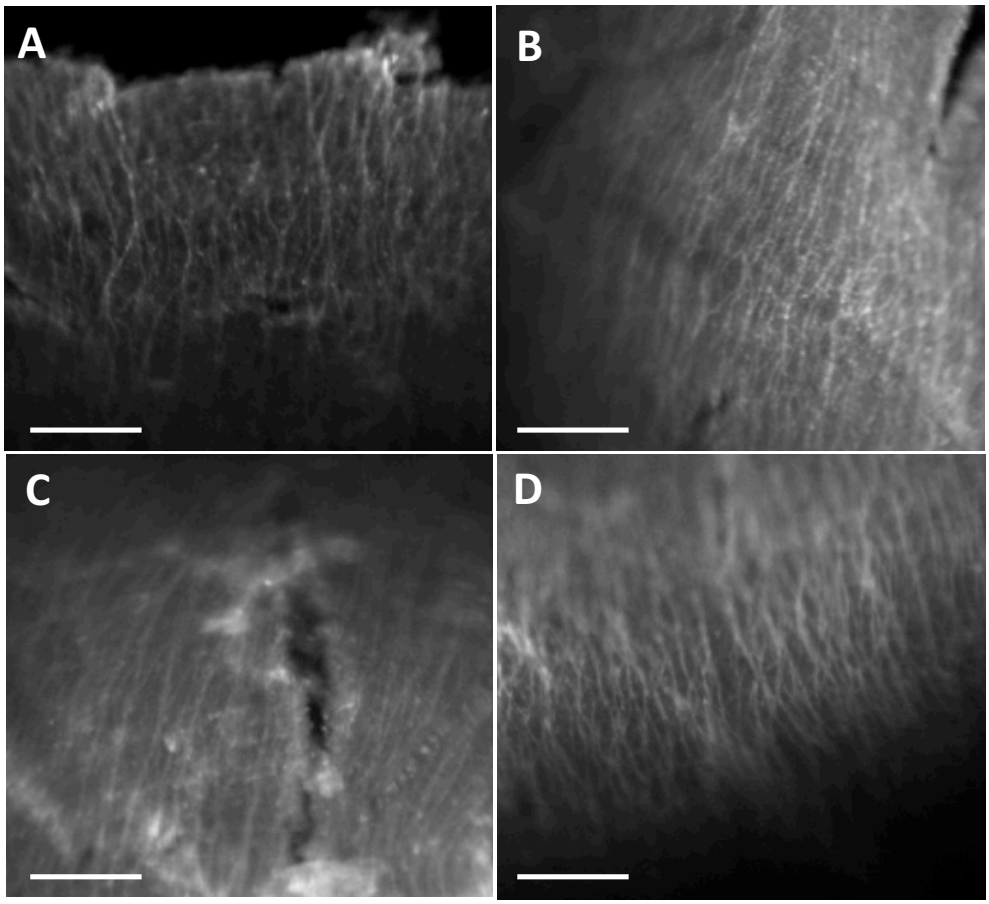

Figure 21. P-NF staining of retina flat-mount showed approximately 1 µm thick axons under cSLO-IRAF

All panels are showing cSLO-IRAF images after staining of the retina flat-mount.
(A)-(B) are from two ALS patients. (A) 72 y/o male; (B) 71 y/o female;
(C)-(D) are from two control patients. (C) 43 y/o female; (D) 66 y/o male

Segments of stronger signal with larger diameter can be seen along the length of the axons.

Scale bar = 400 µm

4.3.2. IMS imaging

IMS images with a NIRF filter were captured for the same flat-mounted retinal tissue that was previously imaged with cSLO. Segments of enlarged axons with higher signal were also observed along each axon. Co-registration between the two imaging systems confirmed that the structures observed in the cSLO-IRAF images were the same ones in the IMS images. In general, the signal was stronger in IMS than in cSLO which could explain the better imaging resolution of IMS (Figure 22)

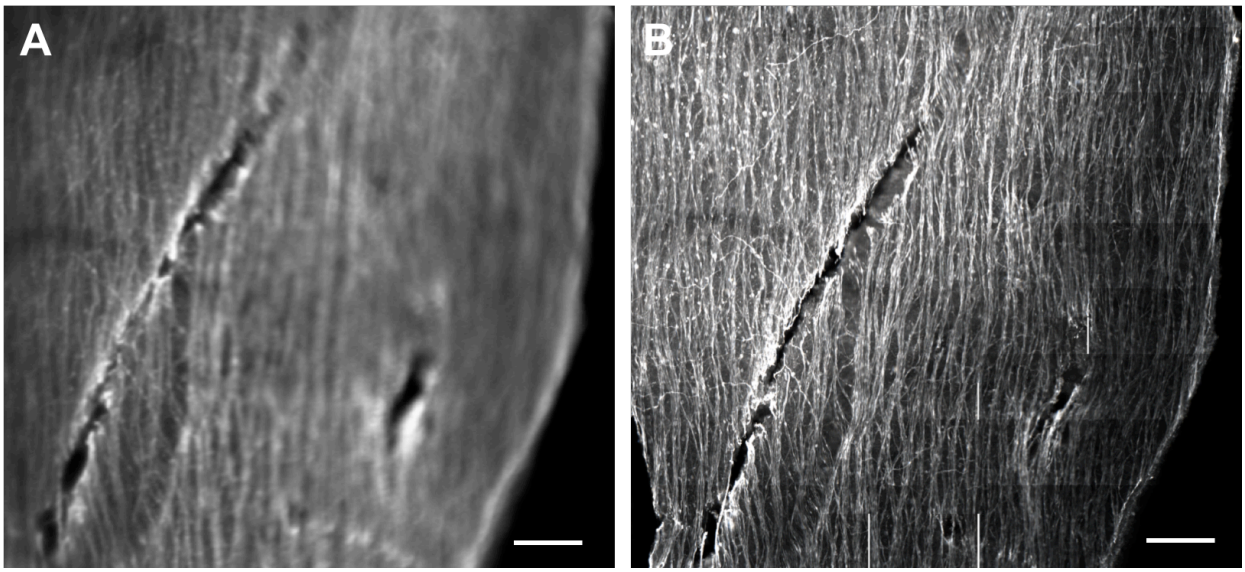

Figure 22. IMS confirmed cSLO-IRAF finding with higher resolution

(A) cSLO-IRAF image of a retina flat-mount from a 71 years old ALS female after staining. The images is taken with 90D lens at 15 degree scanning angle. cSLO-IRAF showed same structures as in (B) IMS image of the same patient. The images of IMS were at higher resolution compared to those of cSLO.

Scale bar = 200μm

5. DISCUSSION

Using post-mortem human eyes in this study allowed us to carry histological analysis. The histopathological analysis of the retina tissue of ALS patients showed evidence of axonal pathology in the axons of RGCs. The round bodies in the RNFL observed in PAS-stained retina were confirmed by the immunofluorescence study of phosphorylated neurofilament (P-NF) that showed the accumulation of P-NF in RGC axons in ALS retinas. In addition, there was significantly higher P-NF immunoreactivity in the RNFL of the ALS patients compared to the control patients suggesting alteration of axonal transport in RGC axons in ALS patients. This suggests that axonal pathology does not only affect the motor neurons in the brain and spinal cord but also affects the retinal ganglion cells with long axons.

In fact, a higher level of P-NF was also found in the spinal motor neuron of ALS transgenic mice [23] and cerebrospinal fluid (CSF) and serum of ALS patient [108]. In addition to elevated P-NF, there are other studies suggesting accumulation of P-NF in the motor neurons of the spinal cord of ALS patients [109-113] and transgenic mice with dysfunctional microtubule-associated motor proteins [16, 114-116]. A previous study showed swelling of axons in spinal motor neurons of ALS patients. Electron microscopy also confirmed the swelling to be filled with neurofilaments [109].

Studies have shown similarities in functionality and anatomy of the retina with brain and spinal cord [117, 118]. In addition, researchers have detected some ocular pathology from neurodegenerative processes characterized in CNS disorders [119]. Accumulation of proteins and organelles in motor neurons with long axons is most likely due to altered axonal transport. RGCs also have long axons, and similar mechanism of axonal transport

defect may lead to accumulation of proteins along their axons. Therefore, retinal imaging can be used as a non-invasive tool to monitor axonal pathology in patients with some brain and spinal cord diseases.

The second phase of this study was to assess whether commercially available non-invasive cSLO and OCT retinal imaging techniques can detect axonal pathology in ALS retina. cSLO reflectance images of the whole globe showed hyper-reflective profiles in the retina of ALS patients. There was a higher number of these profiles in ALS patients compared to the age-matched controls. Interestingly, our whole globe retinal imaging results were consistent with the findings of Scoles and co-workers [103]. Using adaptive optics and scanning laser ophthalmoscopy (AOSLO) in patients with retinal or neurologic diseases and normal volunteers, they described similar size hyper-reflective profiles in retinal nerve fiber layer (RNFL) [103].

To further investigate the location of hyper-reflective profiles we performed OCT imaging of the retina. OCT images confirmed that the profiles are mainly located in the RNFL. The shape, size, and location of these profiles were consistent with the morphology and the location of round profiles found in PAS-stained and P-NF immunostained retina section. Large range of hyper-reflective profiles counted form cSLO-BR images of ALS eyes can be due to the heterogeneous genetic and clinical features of ALS in our study [120].

The noninvasive retinal imaging findings of this study demonstrate the potential of cLSO for detecting and monitoring pathological changes in the retina of ALS patients. However, future research is needed for further characterization of these profiles.

Most of the researchers studying the ocular biomarkers for ALS, focused on measuring the retina thickness without other ocular biomarkers. Previous studies measuring retinal thickness with OCT in ALS patients showed no consistent results. There are studies suggesting significant thinning of RNFL and inner nuclear layer in ALS compared to controls [32, 104]. On the other hand, Roth and coworkers found that there is no significant difference in the thickness of retinal layers in ALS patients compared to control patients [33]. In our study, rather than assessing global retinal parameters such as retinal thickness, we studied the specific pathological changes in the axons of the RGCs, in ALS patients with a confirmed clinical and neuropathological diagnosis.

To be able to better understand and correlate these axonal changes, we developed a protocol for human retina flat-mount immunofluorescence staining of P-NF[107]. We were able to show for the first time that axons with 1μm diameter can be visualized in P-NF immunofluorescence stained flat-mount retina using cSLO-IRAF and IMS imaging. Image of axons was captured at higher resolution with IMS but faster and lower resolution with cSLO. This finding suggests that cLSO imaging will be ideal for fast screening of the retina. In addition to detailed fluorescence imaging, IMS can be also used for in-depth spectral analysis of the axons and their cargos. Enlarged segments with stronger signals from both imaging modalities were visible along the length of the axons. However, more investigation is needed to validate whether these enlarged segments are axonal swelling due to the accumulation of proteins and organelles or are just cross-overs of multiple axons. Co-registration of hyper-reflective profiles from cSLO-BR before staining with cSLO-IRAF after staining was not possible due to limitations mentioned in section 7. To our knowledge, our study is the first to visualize and study RGCs axons

with human retina fundus imaging. This method will allow researchers to trace and study individual axons in health and in diseases affecting the CNS. With adaptive optics correcting the refractive errors in the patient eye, cSLO can be used in the clinical setting to monitor the axonal pathology and its progression as an ocular biomarker of axonal pathology in ALS patients.

Disease duration and clinical duration had no correlation with either P-NF immunoreactivity or hyper-reflective profiles density. This may be due to the small sample size in our study. Further studies with larger sample size are needed to correlate these ocular findings with clinical aspects of the disease.

While in-vivo studies with larger sample sizes are needed for a final conclusion, the findings reported here represent a novel approach ranging from neuropathological examination to optical imaging of post-mortem retina tissue from ALS patients to develop novel ocular biomarkers for ALS. The eye imaging technology has the potential to visualize and characterize retinal axonal pathology in vivo in the patients with neurodegenerative diseases in a noninvasive manner.

6. CONCLUSION

This is the first study to systematically image post-mortem retinas of ALS patients compared to age-matched controls. The study provides evidence of lesions in the RNFL of the ALS patients. Histopathology study of the retina sections showed axonal pathology in the retina of ALS patients. Round profiles present in the RNFL of ALS patients by PAS staining as well as the accumulation of P-NF and increased P-NF immunoreactivity in the RNFL of ALS retina suggest that axonal pathology occurs in the retina of ALS patients. These changes were detected as hyper-reflective profiles in the retina of ALS patients by blue reflectance cSLO and OCT imaging modalities. The results of this study point to a novel potential biomarker for ALS that can be detected using eye imaging.

7. LIMITATIONS OF STUDY AND FUTURE DIRECTIONS

Although our findings from this study are very promising, we acknowledge that this study also has some limitations. The first limitation comes from the use of post-mortem human eye. We were not able to carry the study at a different time point during the disease progression. However, post-mortem specimen allows us to carry out histology studies of the retina. In addition, quality of in-vivo cSLO and OCT imaging are better comparing to post-mortem imaging but this was not a big issue for our study due to the high digital resolution of the Spectralis system used for this study which can make up part of this drawback. The OCT imaging has a resolution of 3.9 μm axially x 11 μm laterally and the cSLO imaging has the resolution of 6 μm/pixel. Also, we did not use

OCT to measure the thickness of the retina layers but it was used to validate the presence of hyper-reflective profiles in the cSLO images.

Although, the sample size was adequate to show there is a significant difference in our findings between the ALS and control groups the second limitation of this study is the sample size. To perform a multivariate analysis of the parameters of eye imaging and clinical characteristics larger sample size is required.

The third limitation was choosing optimal age-matched control eyes. The control patients are those who died of an unrelated disease or illness and they were not healthy control patients. The fact that the round profiles were present in both ALS and some control patients with higher density in ALS, suggests that some of these changes may be due to aging or other comorbid conditions.

Another limitation of this study was co-registration of hyper-reflective profiles seen from cSLO-BR images of the retina flat-mount before staining with profiles seen from cSLO-IRAF after staining. These could be due to few factors involved during staining and imaging process. The first factor is the thick tissue staining and the use of Triton, a detergent used to open pores into the cell membrane and allowing antibody penetration, for longer incubation time and at higher concentration. Triton could dissolve some of the molecules in the cell and change the optical property of the tissue. The second factor is due to change in angle and position of the Spectalis camera between before and after staining imaging. Keeping the camera angle fixed was not possible due to modifying the angle for imaging more than one piece of the retina at every time. This caused changes in x:y aspect ratio of the tissue before and after staining. In addition, tissue architecture changed during staining and remounting procedures.

Our next goal is to modify imaging and staining protocol, for co-registration of hyper-reflective profiles before staining with profiles after staining. Also, we would like to study the retina of young donors and determine the relationship between our findings and people of different age groups. It will also be ideal to use eyes from patients with other neurodegenerative diseases such as Alzheimer's disease, multiple sclerosis, and Parkinson's disease and determine whether our findings are specific to ALS.

Further investigations are needed to confirm whether the increased density of hyper-reflective profiles in the retina correlates with ALS disease severity and progression, and to validate the clinical utility as a biomarker to assess the disease severity and monitor its progression. Additional neuropathological and molecular studies are needed to determine the nature of round structures and whether they represent the abnormal accumulation of proteins, similar to those seen in the brain and spinal cord of ALS patients. This can be done by using our IMS camera to study the spectral information of hyper-reflective profiles and comparing it with spectral information of the proteins and organelles accumulated in defected axons of neurodegenerative diseases.

Having detailed clinical information, results of neuropathological examination of brain and spinal cord and genetic testing for mutations will allow us to correlate eye imaging and histological findings with clinical observations, neuropathological and genetic findings. This would be very helpful to elucidate the clinical relevance of these retinal changes in ALS disease. Our long-term goal is to adapt existing imaging devices for neurodegenerative disease and explore new eye imaging modalities for clinical trials as a non-invasive way to monitor the progression of the disease and treatment effect.

REFERENCES

1. Chevalier-Larsen, E. and E.L. Holzbaur, *Axonal transport and neurodegenerative disease.* Biochim Biophys Acta, 2006. **1762**(11-12): p. 1094-108.
2. Purves, D. and S.M. Williams, *Neuroscience*. 2nd ed. 2001, Sunderland, Mass: Sinauer Associates.
3. Monro, T.K., *Optic Nerve as Part of the Central Nervous System.* Journal of Anatomy and Physiology, 1895. **30**(Pt 1): p. 45-48.
4. Alberts, B., et al., *Molecular Biology of The Cell*. 2008: Garland Science, Taylor & Francis Group.
5. Lopez, P.H., et al., *Myelin-associated glycoprotein protects neurons from excitotoxicity.* J Neurochem, 2011. **116**(5): p. 900-8.
6. Debanne, D., et al., *Axon physiology.* Physiol Rev, 2011. **91**(2): p. 555-602.
7. Ackerley, S., et al., *Glutamate Slows Axonal Transport of Neurofilaments in Transfected Neurons.* The Journal of Cell Biology, 2000. **150**(1): p. 165-176.
8. Elder, G.A., et al., *Absence of the Mid-sized Neurofilament Subunit Decreases Axonal Calibers, Levels of Light Neurofilament (NF-L), and Neurofilament Content.* The Journal of Cell Biology, 1998. **141**(3): p. 727-739.
9. Miller, C.C.J., et al., *Axonal transport of neurofilaments in normal and disease states.* Cellular and Molecular Life Sciences CMLS, 2002. **59**(2): p. 323-330.
10. Hurd, D.D. and W.M. Saxton, *Kinesin Mutations Cause Motor Neuron Disease Phenotypes by Disrupting Fast Axonal Transport in Drosophila.* Genetics, 1996. **144**(3): p. 1075-1085.
11. Baird, F.J. and C.L. Bennett, *Microtubule defects & Neurodegeneration.* Journal of genetic syndrome & gene therapy, 2013. **4**: p. 203.
12. Gibbs, K.L., L. Greensmith, and G. Schiavo, *Regulation of Axonal Transport by Protein Kinases.* Trends Biochem Sci, 2015. **40**(10): p. 597-610.
13. Maday, S., et al., *Axonal transport: cargo-specific mechanisms of motility and regulation.* Neuron, 2014. **84**(2): p. 292-309.
14. Schroer, T.A., *Dynactin.* The Annual Review of Cell and Developmental Biology, 2004. **20**: p. 759-779.
15. Rao, M.V. and R.A. Nixon, *Defective NF Transport in Mouse Models of ALS.* Neurochemical Research, 2003. **28**(7): p. 1041-1047.
16. Lamonte, B.H., et al., *Disruption of Dynein Dynactin Inhibits Axonal Transport in motor Neurons Causing Late-Onset Progressive Degeneration (ALS).* Neruon, 2002. **34**: p. 715-727.
17. Stokin, G.B., et al., *Axonopathy and Transport Deficits Early in the Pathogenesis of Alzheimer's Disease.* Science, 2005. **307**(5713): p. 1282-1288.
18. Collard, J.-F.C., Francine; Julien, Jean-Pierre, *Defective axonal transport in a transgenic mouse model of amyotrophic lateral sclerosis.* Nature, 1995. **375**(6526): p. 61-4.
19. Chu, Y., et al., *Alterations in axonal transport motor proteins in sporadic and experimental Parkinson's disease.* Brain, 2012. **135**(Pt 7): p. 2058-73.
20. Ishihara, T., et al., *Age-Dependent Emergence and Progression of a Tauopathy in Transgenic Mice Overexpressing the Shortest Human Tau Isoform.* Neuron, 1999. **24**(3): p. 751-762.
21. Griffin, J.W., et al., *Slow Axonal Transport of Neurofilament Proteins: Impairment by β,β'-Iminodipropionitrile Administration.* Science, 1978. **202**(4368): p. 633-635.
22. Chidlow, G., et al., *The optic nerve head is the site of axonal transport disruption, axonal cytoskeleton damage and putative axonal regeneration failure in a rat model of glaucoma.* Acta Neuropathologica, 2011. **121**(6): p. 737-751.
23. Julien, J.-P. and J.-M. Beaulieu, *Cytoskeletal abnormalities in Amyotrophic Lateral Sclerosis: beneficial or detrimental effects?* Journal of Neurological Sciences, 2000. **180**: p. 7-14.

24. Xiao, S., J. McLean, and J. Robertson, *Neuronal intermediate filaments and ALS: a new look at an old question.* Biochim Biophys Acta, 2006. **1762**(11-12): p. 1001-12.
25. Brown, A., et al., *Rapid movement of axonal neurofilaments interrupted by prolonged pauses.* Nature Cell Biology, 2000. **2**(3): p. 137-141.
26. Shea, T.B. and L.A. Flanagan, *Kinesin, dynein and neurofilament transport.* Trends in Neurosciences, 2001. **24**(11): p. 644-648.
27. London, A., I. Benhar, and M. Schwartz, *The retina as a window to the brain-from eye research to CNS disorders.* Nat Rev Neurol, 2013. **9**(1): p. 44-53.
28. Benowitz, L. and Y. Yin, *Rewiring the injured CNS: Lessons from the optic nerve.* Experimental Neurology, 2008. **209**(2): p. 389-398.
29. Vidal-Sanz, M., et al., *Axonal regeneration and synapse formation in the superior colliculus by retinal ganglion cells in the adult rat.* Journal of Neuroscience, 1987. **7**(9): p. 2894-2909.
30. Crair, M.C. and C.A. Mason, *Reconnecting Eye to Brain.* J Neurosci, 2016. **36**(42): p. 10707-10722.
31. Jenkins, T.M. and A.T. Toosy, *Optic neuritis: the eye as a window to the brain.* Curr Opin Neurol, 2017. **30**(1): p. 61-66.
32. Hubers, A., et al., *Retinal involvement in amyotrophic lateral sclerosis: a study with optical coherence tomography and diffusion tensor imaging.* J Neural Transm (Vienna), 2016. **123**(3): p. 281-7.
33. Roth, N.M., et al., *Optical coherence tomography does not support optic nerve involvement in amyotrophic lateral sclerosis.* Eur J Neurol, 2013. **20**(8): p. 1170-6.
34. Gupta, M.P., et al., *Retinal Anatomy and Pathology.* Dev Ophthalmol, 2016. **55**: p. 7-17.
35. Wu, Z., et al., *Impact of Normal Aging and Progression Definitions on the Specificity of Detecting Retinal Nerve Fiber Layer Thinning.* Am J Ophthalmol, 2017. **181**: p. 106-113.
36. Gardiner, S.K., et al., *Changes in Retinal Nerve Fiber Layer Reflectance Intensity as a Predictor of Functional Progression in Glaucoma.* Invest Ophthalmol Vis Sci, 2016. **57**(3): p. 1221-7.
37. Buckingham, B.P., et al., *Progressive ganglion cell degeneration precedes neuronal loss in a mouse model of glaucoma.* J Neurosci, 2008. **28**(11): p. 2735-44.
38. J, M.Y., *Ocular Pathology*. 2015: Elsevier.
39. Heemels, M.-T., *Neurodegenerative diseases.* Nature, 2016. **539**: p. 179.
40. Kiernan, M.C., et al., *Amyotrophic lateral sclerosis.* The Lancet, 2011. **377**(9769): p. 942-955.
41. Klemann, C.J.H.M., et al., *Integrated molecular landscape of amyotrophic lateral sclerosis provides insights into disease etiology: Insights into ALS etiology.* Brain Pathology, 2018. **28**(2): p. 203-211.
42. Magnus, T., et al., *Disease progression in amyotrophic lateral sclerosis: Predictors of survival.* Muscle & Nerve, 2002. **25**(5): p. 709-714.
43. Hardiman, O., L.H. van den Berg, and M.C. Kiernan, *Clinical diagnosis and management of amyotrophic lateral sclerosis.* Nature reviews. Neurology, 2011. **7**(11): p. 639-649.
44. Aguila, M.A.d., *Prognosis in amyotrophic lateral sclerosis: a population-based study.* JAMA, The Journal of the American Medical Association, 2003. **289**(22): p. 2919.
45. Zarei, S., et al., *A comprehensive review of amyotrophic lateral sclerosis.* Surgical Neurology International, 2015. **6**: p. 171.
46. Cedarbaum, J.M., et al., *The ALSFRS-R: a revised ALS functional rating scale that incorporates assessments of respiratory function.* Journal of the Neurological Sciences, 1999. **169**(1): p. 13-21.
47. Zou, Z.Y., et al., *Toward precision medicine in amyotrophic lateral sclerosis.* Ann Transl Med, 2016. **4**(2): p. 27.
48. Brooks, B.R., *El escorial World Federation of Neurology criteria for the diagnosis of amyotrophic lateral sclerosis.* Journal of the Neurological Sciences, 1994. **124**: p. 96-107.

49. Li, H.F. and Z.Y. Wu, *Genotype-phenotype correlations of amyotrophic lateral sclerosis.* Transl Neurodegener, 2016. **5**: p. 3.
50. Turner, M.R., et al., *Controversies and priorities in amyotrophic lateral sclerosis.* The Lancet Neurology, 2013. **12**(3): p. 310-322.
51. Taiana, M., J. Sassone, and G. Lauria, *Mutant SOD1 accumulation in sensory neurons does not associate with endoplasmic reticulum stress features: Implications for differential vulnerability of sensory and motor neurons to SOD1 toxicity.* Neurosci Lett, 2016. **627**: p. 107-14.
52. Joyce, P.I., et al., *A novel SOD1-ALS mutation separates central and peripheral effects of mutant SOD1 toxicity.* Hum Mol Genet, 2015. **24**(7): p. 1883-97.
53. Pratt, A.J., E.D. Getzoff, and J.J. Perry, *Amyotrophic lateral sclerosis: update and new developments.* Degener Neurol Neuromuscul Dis, 2012. **2012**(2): p. 1-14.
54. Ajroud-Driss, S. and T. Siddique, *Sporadic and hereditary amyotrophic lateral sclerosis (ALS).* Biochim Biophys Acta, 2015. **1852**(4): p. 679-84.
55. O'Rourke, J.G., et al., *C9orf72 is required for proper macrophage and microglial function in mice.* Science (New York, N.Y.), 2016. **351**(6279): p. 1324-1329.
56. Rutherford, N.J., et al., *Novel mutations in TARDBP (TDP-43) in patients with familial amyotrophic lateral sclerosis.* PLoS Genet, 2008. **4**(9): p. e1000193.
57. Grillo, F.W., et al., *Chapter 11 - In Vivo Visualization of Single Axons and Synaptic Remodeling in Normal and Pathological Conditions*, in *Axons and Brain Architecture*, K.S. Rockland, Editor. 2016, Academic Press: San Diego. p. 221-243.
58. Budde, M.D., et al., *Axonal injury detected by in vivo diffusion tensor imaging correlates with neurological disability in a mouse model of multiple sclerosis.* NMR in Biomedicine, 2008. **21**(6): p. 589-597.
59. Verstraete, E., et al., *Mind the gap: the mismatch between clinical and imaging metrics in ALS.* Amyotroph Lateral Scler Frontotemporal Degener, 2015. **16**(7-8): p. 524-9.
60. Miller, R.G., J.D. Mitchell, and D.H. Moore, *Riluzole for amyotrophic lateral sclerosis (ALS)/motor neuron disease (MND).* Cochrane Database Syst Rev, 2012(3): p. CD001447.
61. Chiò, A., et al., *Neuroimaging in amyotrophic lateral sclerosis: insights into structural and functional changes.* The Lancet Neurology, 2014. **13**(12): p. 1228-1240.
62. Artal, P., *Handbook of Visual Optics - Fundamentals and Eye Optics (Volume I)*. 2017: Taylor & Francis Group.
63. R.D, G., *Phototoxicity to the Retina: Mechanisms of Damage.* International Journal of Toxicology, 2002. **21**(6): p. 473-490.
64. Yust, B.G., L.C. Mimun, and D.K. Sardar, *Optical absorption and scattering of bovine cornea, lens, and retina in the near-infrared region.* Lasers in Medical Science, 2012. **27**(2): p. 413-422.
65. Abramoff, M.D., et al., *Visual Stimulus-Induced Changes in Human Near-Infrared Fundus Reflectance.* Investigative Ophthalmology & Visual Science, 2006. **47**(2): p. 715-721.
66. Tsunoda, K., et al., *Mapping Cone- and Rod-Induced Retinal Responsiveness in Macaque Retina by Optical Imaging.* Investigative Ophthalmology & Visual Science, 2004. **45**(10): p. 3820.
67. Hanazono, G., et al., *Intrinsic Signal Imaging in Macaque Retina Reveals Different Types of Flash-Induced Light Reflectance Changes of Different Origins.* Investigative Ophthalmology & Visual Science, 2007. **48**(6): p. 2903.
68. Sardar, D.K., et al., *Optical absorption and scattering of bovine cornea, lens and retina in the visible region.* Lasers in medical science, 2009. **24**(6): p. 839-847.
69. Abramoff, M.D., M.K. Garvin, and M. Sonka, *Retinal imaging and image analysis.* IEEE Rev Biomed Eng, 2010. **3**: p. 169-208.
70. Cheung, N., et al., *Retinal fractals and acute lacunar stroke.* Ann Neurol, 2010. **68**(1): p. 107-11.

71. Wong, T.Y., et al., *Relation of retinopathy to coronary artery calcification: the multi-ethnic study of atherosclerosis.* Am J Epidemiol, 2008. **167**(1): p. 51-8.
72. Fleckenstein, M., S. Schmitz-Valckenberg, and F.G. Holz, *Chapter 4 - Autofluorescence Imaging*, in *Retina (Fifth Edition)*, S.J. Ryan, et al., Editors. 2013, W.B. Saunders: London. p. 111-132.
73. Kim, J., et al., *Functional Optical Coherence Tomography: Principles and Progress.* Physics in medicine and biology, 2015. **60**(10): p. R211-R237.
74. Huang, D., et al., *Optical coherence tomography.* Science, 1991. **254**(5035): p. 1178-1181.
75. Fujimoto, J.G., *Optical coherence tomography.* Comptes Rendus de l'Académie des Sciences - Series IV - Physics, 2001. **2**(8): p. 1099-1111.
76. Coscas, G., F. Coscas, and S. Vismara, *Optical Coherence Tomography in Age-Related Macular Degeneration*. 2009: Springer, Berlin, Heidelberg.
77. Neri, A., et al., *Retinal thickness analysis with time and spectral-domain optical coherence tomography. Cross-platform interchangeability of manual measurements.* Acta bio-medica : Atenei Parmensis, 2011. **82**(3): p. 244.
78. de Carlo, T.E., et al., *A review of optical coherence tomography angiography (OCTA).* International journal of retina and vitreous, 2015. **1**(1): p. 5.
79. Novotny, H.R. and D.L. Alvis, *A method of photographing fluorescence in circulating blood in the human retina.* Circulation, 1961. **24**(1): p. 82-86.
80. Bedard, N., et al., *Image mapping spectrometry: calibration and characterization.* Opt Eng, 2012. **51**(11).
81. Oke, J.B., et al., *The Keck Low-Resolution Imaging Spectrometer.* Publications of the Astronomical Society of the Pacific, 1995. **107**(710): p. 375-385.
82. Vane, G., et al., *The airborne visible/infrared imaging spectrometer (AVIRIS).* Remote Sensing of Environment, 1993. **44**(2): p. 127-143.
83. Gowen, A., et al., *Hyperspectral imaging – an emerging process analytical tool for food quality and safety control.* Trends in Food Science & Technology, 2007. **18**(12): p. 590-598.
84. Zimmermann, T., J. Rietdorf, and R. Pepperkok, *Spectral imaging and its applications in live cell microscopy.* FEBS Letters, 2003. **546**(1): p. 87-92.
85. Gao, L., et al., *Snapshot Image Mapping Spectrometer (IMS) with high sampling density for hyperspectral microscopy.* Optics express, 2010. **18**(14): p. 14330.
86. Gao, L., R.T. Kester, and T.S. Tkaczyk, *Compact Image Slicing Spectrometer (ISS) for hyperspectral fluorescence microscopy.* Optics express, 2009. **17**(15): p. 12293.
87. Kester, R.T., L. Gao, and T.S. Tkaczyk, *Development of image mappers for hyperspectral biomedical imaging applications.* Applied Optics, 2010. **49**(10): p. 1886.
88. Elliott, A.D., et al., *Real-time hyperspectral fluorescence imaging of pancreatic beta-cell dynamics with the image mapping spectrometer.* J Cell Sci, 2012. **125**(Pt 20): p. 4833-40.
89. Hagen, N., et al., *Spectrally-resolved imaging of dynamic turbid media.* 2011. **7892**: p. 789206.
90. Kester, R.T., et al., *Real-time snapshot hyperspectral imaging endoscope.* Journal of Biomedical Optics, 2011. **16**(5): p. 056005-056005.
91. Stucht, D., et al., *Highest Resolution In Vivo Human Brain MRI Using Prospective Motion Correction.* PLoS One, 2015. **10**(7): p. e0133921.
92. Mainardi, L., et al., *Understanding atrial fibrillation: the signal processing contribution*. Vol. 24-25.;24 & #25;. 2008, San Rafael, CA: Morgan & Claypool Publishers.
93. Gupta, A., et al., *Accuracy of Conventional MRI in ALS.* Canadian Journal of Neurological Sciences / Journal Canadien des Sciences Neurologiques, 2014. **41**(01): p. 53-57.
94. Granov, A.M., et al., *Positron Emission Tomography*. 1. Aufl.;1st; ed. 2013, Berlin, Heidelberg: Springer Berlin Heidelberg.

95. Catafau, A.M. and S. Bullich, *Amyloid PET imaging: applications beyond Alzheimer's disease.* Clin Transl Imaging, 2015. **3**(1): p. 39-55.
96. Montgomery, A.J., et al., *Correction of Head Movement on PET Studies: Comparison of Methods.* The Journal of Nuclear Medicine, 2006. **47**(12): p. 1936.
97. Salmon, E., C. Bernard Ir, and R. Hustinx, *Pitfalls and Limitations of PET/CT in Brain Imaging.* Semin Nucl Med, 2015. **45**(6): p. 541-51.
98. Simao, L.M., *The contribution of optical coherence tomography in neurodegenerative diseases.* Curr Opin Ophthalmol, 2013. **24**(6): p. 521-7.
99. Yu, J.G., et al., *Retinal nerve fiber layer thickness changes in Parkinson disease: a meta-analysis.* PLoS One, 2014. **9**(1): p. e85718.
100. *<Uchida et al. 2018 Outer Retinal Assessment Using Spectral-Domain OCT in Patients With Alzheimer's and Parkinson's Disease.pdf>.*
101. Svetozarskiy, S.N. and S.V. Kopishinskaya, *Retinal Optical Coherence Tomography in Neurodegenerative Diseases (Review).* Sovremennye tehnologii v medicine, 2015. **7**(1): p. 116-123.
102. Tsironi, E.E., et al., *Perimetric and retinal nerve fiber layer findings in patients with Parkinson's disease.* BMC ophthalmology, 2012. **12**(1): p. 54-54.
103. Scoles, D., et al., *Microscopic inner retinal hyper-reflective phenotypes in retinal and neurologic disease.* Invest Ophthalmol Vis Sci, 2014. **55**(7): p. 4015-29.
104. Mukherjee, N., et al., *Retinal thinning in amyotrophic lateral sclerosis patients without ophthalmic disease.* PloS one, 2017. **12**(9): p. e0185242.
105. Burke, M., et al., *The Gateway to the Brain: Dissecting the Primate Eye.* Journal of Visualized Experiments, 2009(27).
106. Knight, K. *Immunohistochemistry Protocol for Paraffin-Embedded Sections*. 2016; Available from: https://www.biolegend.com/protocols/immunohistochemistry-protocol-for-paraffin-embedded-sections/4256/.
107. Wang, L., et al., *Varicosities of intraretinal ganglion cell axons in human and nonhuman primates.* (0146-0404 (Print)).
108. Weydt, P., et al., *Neurofilament levels as biomarkers in asymptomatic and symptomatic familial amyotrophic lateral sclerosis.* Annals of Neurology, 2016. **79**(1): p. 152-158.
109. Delisle, M.B. and S. Carpenter, *Neurofibrillary Axonal Swellings and Amyotrophic Lateral Sclerosis.* Journal of Neurological Sciences, 1984. **63**(2): p. 241-250.
110. Julien, J.-P., *A role for neurofilaments in the pathogenesis of amyotrophic lateral sclerosis.* Biochemistry and Cell Biology, 1995. **73**(9-10): p. 593-597.
111. Munoz, D.G., et al., *Accumulation of Phosphorylated Neurofilaments in Anterior Horn Motoneurons of Amyotrophic Lateral Sclerosis Patients.* Journal of Neuropathology and Experimental Neurology, 1988. **47**(1): p. 9-18.
112. Leigh, P.N., et al., *Cytoskeletal Abnormalities in Motor Neuron Disease.* 1989. **112**: p. 521-535.
113. Murayama, S., T.W. Bouldin, and K. Suzuki, *Immunocytochemical and ultrastructural studies of upper motor neurons in amyotrophic lateral sclerosis.* Acta neuropathologica, 1992. **83**(5): p. 518-524.
114. Laird, F.M., et al., *Motor Neuron Disease Occurring in a Mutant Dynactin Mouse Model Is Characterized by Defects in Vesicular Trafficking.* Journal of Neuroscience, 2008. **28**(9): p. 1997-2005.
115. Xia, C.-H., et al., *Abnormal Neurofilament Transport Caused by Targeted Disruption of Neuronal Kinesin Heavy Chain KIF5A.* The Journal of Cell Biology, 2003. **161**(1): p. 55-66.
116. Koehnle, T.J. and A. Brown, *Slow Axonal Transport of Neurofilament Protein in Cultured Neurons.* The Journal of Cell Biology, 1999. **144**(3): p. 447-458.

117. Streilein, J.W., *Ocular immune privilege: therapeutic opportunities from an experiment of nature.* Nature Reviews Immunology, 2003. **3**(11): p. 879-889.
118. Kaur, C., W.S. Foulds, and E.A. Ling, *Blood–retinal barrier in hypoxic ischaemic conditions: Basic concepts, clinical features and management.* Progress in Retinal and Eye Research, 2008. **27**(6): p. 622-647.
119. London, A., I. Benhar, and M. Schwartz, *The retina as a window to the brain-from eye research to CNS disorders.* Nature reviews. Neurology, 2013. **9**(1): p. 44-53.
120. Beghi, E., et al., *The heterogeneity of amyotrophic lateral sclerosis: a possible explanation of treatment failure.* (0929-8673 (Print)).